Battery-free Wireless Sensor Network For Advanced Fossil-Fuel Based Power Generation

Final Report

Reporting Period Start Date: March 1, 2007
Reporting Period End Date: March 30, 2011

Principal Author: Yi Jia

Mechanical Engineering Department
University of Puerto Rico Mayagüez Campus
Mayagüez, PR 00682-9045

Phone: (787) 832-4040 ext. 3482, Fax: (787) 265-3817
Email: yi.jia@upr.edu

DOE Award No: DE-FG26-07NT43061

February 18, 2012

Disclaimer

Abstract

This report summarizes technical progress achieved during the project supported by the Department of Energy under Award Number DE-FG26-07NT4306. The aim of the project was to conduct basic research into battery-free wireless sensing mechanism in order to develop novel wireless sensors and sensor network for physical and chemical parameter monitoring in a harsh environment. Passive wireless sensing platform and five wireless sensors including temperature sensor, pressure sensor, humidity sensor, crack sensor and networked sensors developed and demonstrated in our laboratory setup have achieved the objective for the monitoring of various physical and chemical parameters in a harsh environment through remote power and wireless sensor communication, which is critical to intelligent control of advanced power generation system. This report is organized by the sensors developed as detailed in each progress report.

Table of Contents

Abstract 3
1. Executive Summary 6
2. Passive Wireless Temperature Sensor 6
2.1 Overall sensor structure design 6
2.2 Identify critical design parameters 6
2.3 First order capacitive sensing element Model 7
2.4 Inductor coil model 7
2.5 Design simulation results 9
2.5.1 Inductance of spiral inductor coil 9
2.5.2 Capacitance of sensing element 9
2.5.4 Results and discussition 12
2.6 High Temperature Sensing Materials 13
2.6.1 Technical approach 13
2.6.2 High temperature ceramic materials 13
2.6.3 Piezoelectric Materials 16
2.6.4 Material selection and characterization 18
2.6.5 Results and discussions 19
2.7 Passive wireless temperature sensor design 19
2.7.1 Sensor Design and Simulation 20
2.7.2 Performance Analysis: Electrical Model 22
2.7.3 Performance Analysis : *Q*-factor 25
2.7.4 Performance Analysis: *Coupling Factor* 25
2.7.5 Results and discussions 26
2.8 Sensor fabrication and calibration 27
2.9 Results and discussions 29
2.10 Application to temperature monitoring of a rotational component 29
2.10.1 Results and Discussions 30
2.10.2 Conclusions 31
3. Passive Wireless Pressure Sensor 32
3.1 Introduction 32
3.2 Principle of operation 32
3.3 Sensor Modeling 35
3.3.1 Capacitance estimation 36
3.3.2 Inductance estimation 40

3.3 Sensor fabrication and experimental results 41
3.3.1 Calibration Results of Parallel Plate Pressure Sensors 41
3.4 Conclusion 43
4. RFID based passive wireless humidity sensor 44
4.1 Principles of Operation 44
4.2 RFID Humidity Sensing Tag 45
4.3 Experimental Details 46
4.4 Results and discussions 47
5. Zigbee enable wireless temperature sensor network 49
5.1 Introduction 49
5.2 Network Hardware Design 51
5.2.1 Sensing Unit 51
5.2.2 Sensor Interface Unit 51
5.2.3 Wireless Communication Unit 52
5.2.4 Power Unit 53
5.3 Evaluation Results 53
5.4 Conclusions 54
A. Network Architecture Design 55
B. Network Hardware Design 55
C. Network Software Design 56
6. Preliminary study of passive wireless crack sensor 58
6.1 Introduction 58
6.2 Crack sensor model 59
6.2.1 Capacitance estimation 59
7. List of students supported and participated in this project 63
8. List of journal and conference papers published by the results of the project 64

1. Executive Summary

This research project has focused on wireless temperature sensing platform design and extended this platform to various physical and humidity sensor developments. First, overall temperature sensor structure was designed and a group of critical design parameters, which determine the sensor design and its performance, were identified. These parameters include sensor geometry parameters, material and its electric property parameters and sensor performance parameters. Second, first order capacitive sensing element model and inductor coil model were developed to prepare sensor design analysis, and finally, an inductor-capacitor resonant circuit based passive wireless sensing platform design was developed and five sensors have been demonstrated.

2. Passive Wireless Temperature Sensor

2.1 Overall sensor structure design

An overall schematic structure of the proposed wireless temperature sensor is shown in Fig. 1. The sensor consists of two parts: inductor coil 1 and temperature sensing capacitor 2. The stack of multi-layer ceramic thick film with capacitive temperature sensing layer 4 is enclosed by two electrodes, 3 and 5, which form a capacitor sensing element, and then the capacitor should be electrically connected to a planar spiral inductor coil 1 through via 7. These two components build up a temperature dependent passive L-C resonator with resonant frequency ω_o, given in Eq. (1).

$$\omega_o = \frac{1}{\sqrt{L_S C_S}} \tag{1}$$

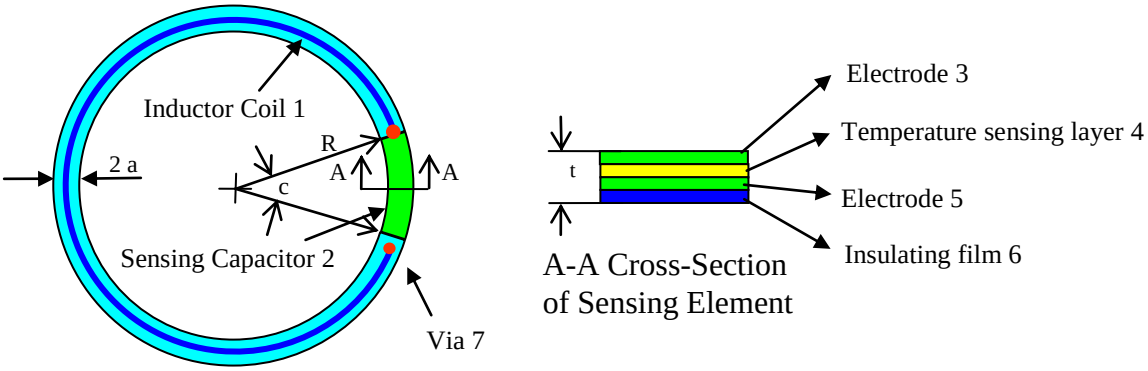

Figure 1. The schematic structure of the wireless temperature sensor

2.2 Identify critical design parameters

Identify critical parameters that determine the sensor geometrical design, material selection, and performance etc., some of the parameters are shown in Figures 1.and 2.

A Area of capacitor electrode plate

a	Half width of the sensor ring
b	Inductor coil thickness
c	The central angle of our proposed sensor
t	Distance between the electrode plates
f	Resonant frequency.
ε_0	Permittivity of free space
ε_r	Relative dielectric constant
r	Inner radius of our proposed sensor
R	Outer radius of our proposed sensor
n	Number of turns of coil
w	Turn width of coil
s	turn spacing of coil
d_{out}	The outer diameter
d_{in}	Inner diameter
d_{avg}	Average diameter of coil
l	Coil lenth
M_0	Magnetic permeability of free space $4\pi \times 10^{-7}$ H/m

2.3 First order capacitive sensing element Model

A first order model of the capacitive sensing element of the temperature sensor is a simple parallel plate capacitor integrated with the dielectric ceramic sensing material, as shown in Fig. 2. The plates of the capacitor consist of conductive films deposited on both sides of the ceramic sensing element material. The capacitance of the parallel-plate capacitor is given by:

$$C = \frac{\varepsilon_0 \varepsilon_r A}{t} \tag{2}$$

$$A = \frac{1}{2}\left(R^2 - r^2\right)c \tag{3}$$

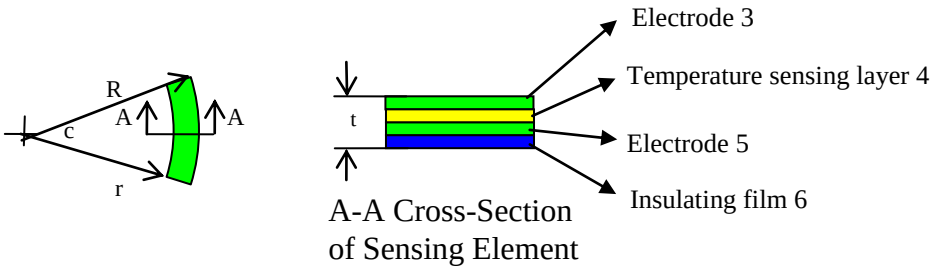

Figure 2. Parallel plate capacitive sensing element

Since dielectric constant of the ceramic material and sensor size play vital roles in the sensor development, the sensor operating frequency as a function of dielectric constant and sensor size A will be studied by employing the formula (1) – (3).

2.4 Inductor coil model

A spiral coils will be incorporated with sensor design based on the ease of its layout. As a power receiving and data transmission element, the planar spiral inductor also governs the sensor characteristics, such as the bandwidth, *Q* factor and the resonant frequency. A spiral layout is shown in Fig. 3. The inductor is specified by the number of turns, N, the track width W, the gap spacing between the coils, S, and one of the following parameters: the outer diameter d_{out}, the inner diameter d_{in}, the average diameter $d_{avg}=0.5(d_{out}+d_{in})$, or the fill ratio, defined as $\rho=(d_{out}-d_{in})/(d_{out}+d_{in})$. Throughout the project, the effects of these parameters on the sensor performance will be studied.

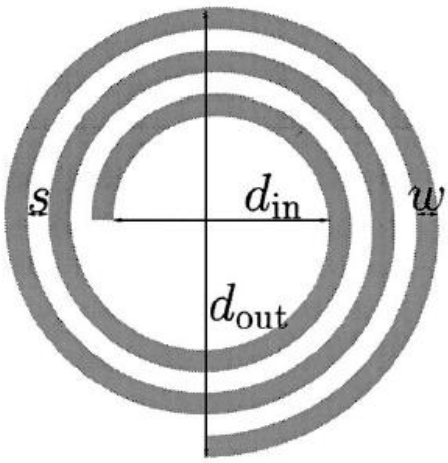

Figure 3. Layout of inductor coil

The inductance *L* can be modeled by the sensor geometry using following equation:

$$L = 1.39\times10^{-6}\left(d_{out}+d_{in}\right)N_L^{5/3}\log_{10}\left(\frac{4\,d_{out}+d_{in}}{d_{out}-d_{in}}\right) \quad (4)$$

The sensor operating frequency and overall performance depend on capacitance of sensing element and inductance of spiral coil in the sensor LC tank. The capacitance and the inductance with a wide range of sensor geometric parameters were simulated. The relationship between sensor performance parameters: capacitance, inductance and operating frequency, and sensor geometric parameters were studied. Based on the desired center operating frequency from 10 MHz to 20 MHz, possible design parameters were illustrated in the Figures 1 and 3. The results have shown that the inductance is in the order of micro Henry and the number of turns in the spiral coil has greater impact on the value of inductance. For the capacitance of sensing element, the dielectric constant and thickness have larger influence for sensor design.

With given dielectric constant and thickness of sensing material, sensor design for a desired center operating frequency can be achieved by changing the diameter of sensor and size of sensing area.

During this period of the research, we also started a pressure sensor design in early September. The research has been focusing on analyzing two different cavity structures for pressure sensing and determining relationship between the cavity structural parameters and pressure induced capacitance change in the sensing element. This is still on-going research and the detailed results will be reported in the next progress report.

2.5 Design simulation results

The sensor operating frequency and overall performance depend on capacitance of sensing element and inductance of spiral coil in the sensor LC tank. In order to design the sensor, the relationship of inductance and capacitance with various sensor geometric parameters were studied, respectively, and the operating frequency is determinated later by using Eq. (1).

$$\omega_o = \frac{1}{\sqrt{L_s C_s}} \tag{1}$$

2.5.1 Inductance of spiral inductor coil

The spiral inductor coil in the proposed sensor acts as a transformer based on the principle of electromagnetic induction. When an oscillating current is executed on the reader antenna, an alternating voltage of the same frequency is induced in the spiral inductor coil as sensor power source. Meanwhile, the frequency change of the LC tank due to the environmental temperature variations can be detected from reader by monitoring the impedance across the reader antenna.

For a circle loop inductor coil, the analytical model was given in first progress report, the relationship between the inductance of the inductor and its geometric parameters was studied. The maximum number of turns was 5 and possible sensor radiuses were calculated from 5 mm to 100 mm. As result shown in Figure 1, the inductance is in the order of micro Henry and the number of turns has greater impact on the value of inductance.

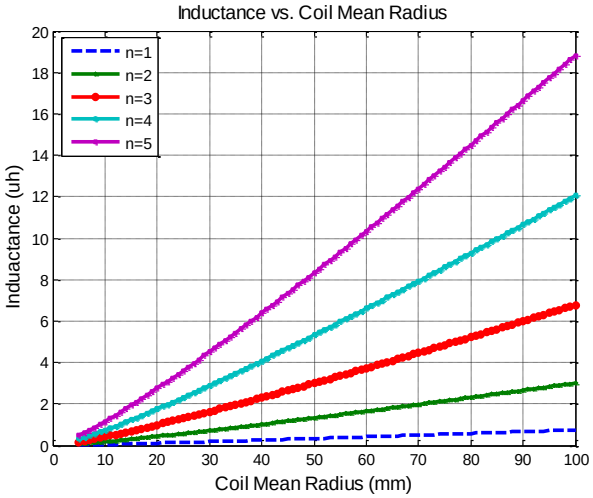

Figure 1. Inductance of spiral coil

2.5.2 Capacitance of sensing element

The planar capacitive sensing element, as shown in Figure 2, stores separated electric charges, and the charge *Q* stored on the capacitor is proportional to the voltage drop across the capacitor given in Eq.(2)

$$Q=C\,V \tag{2}$$

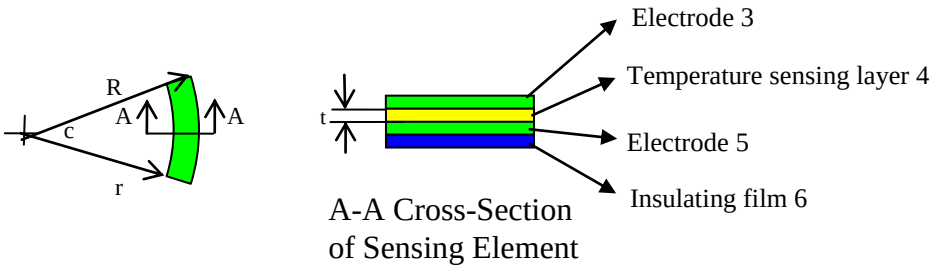

Figure 2. Parallel plate capacitive sensing element

The capacitance of the sensing element is a function of sensing area A, thickness t of dielectric sensing material between two parallel electrodes and dielectric constant $\varepsilon_r(T)$ or the relative permittivity of sensing material. For a sensor fabrication, the sensing area A is easy to control, therefore, the capacitance of the parallel-plate capacitor mainly depends on the dielectric constant and thickness of sensing material seen in Eq (3).

$$C_S(T) = \frac{\varepsilon_0 \varepsilon_r(T) A}{t} \tag{3}$$

We assumed different dielectric constant values of sensing materials from 10 to 300 and then varied its thickness from 5 μm to 60 μm to design the sensor center operating frequency in the range of 10 MHz to 25 MHz. With given dielectric constant and thickness of sensing material, desired center operating frequency can be achieved by changing the diameter of sensor and size of sensing area. The relationship between capacitance and dielectric constant and thickness are illustrated in Figure 3.

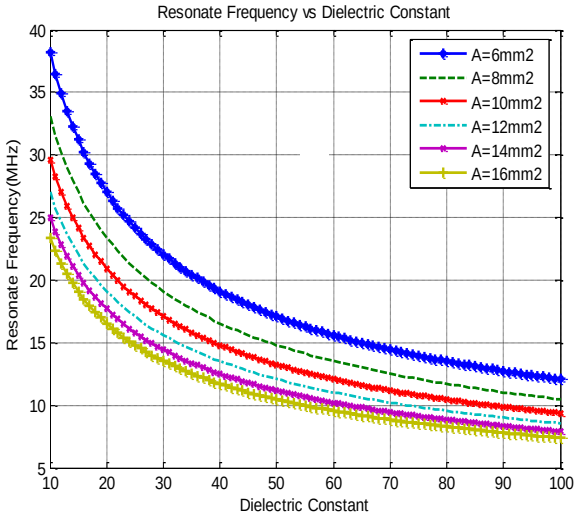

(a) Coil: N=1, R=25mm, thickness t=5um

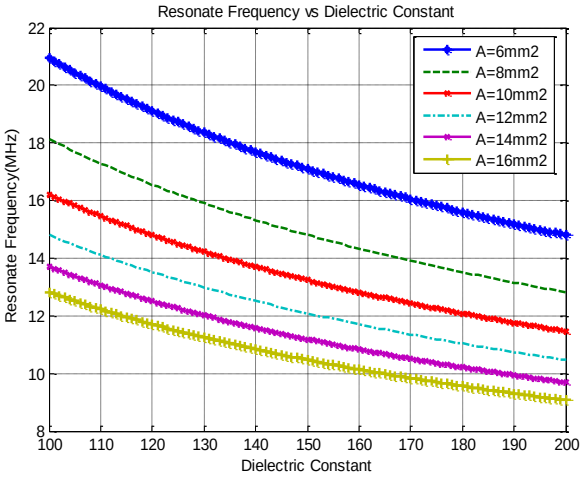

(b) Coil: N=1, R=25mm, thickness: t=15um

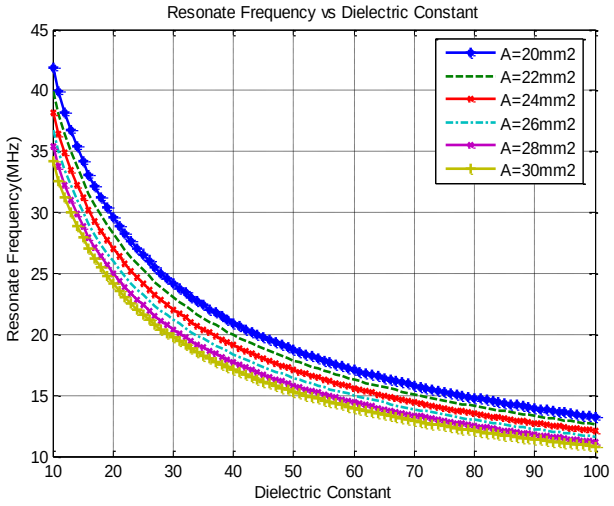

(c) Coil: N=1, R=25mm; thickness t=20um

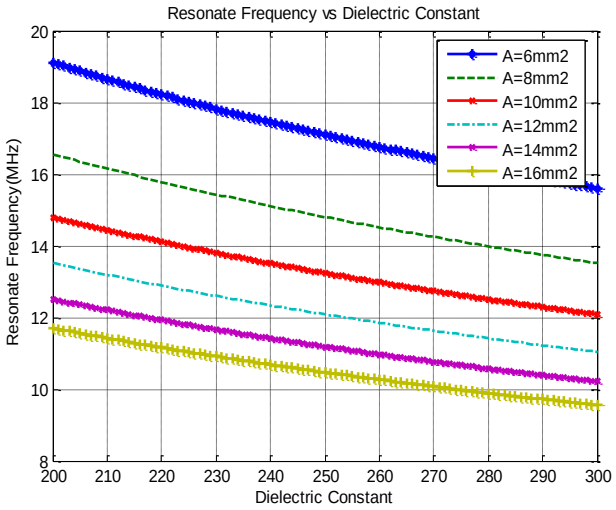

(d) Coil: N=1, R=25mm; Thickness t =25um

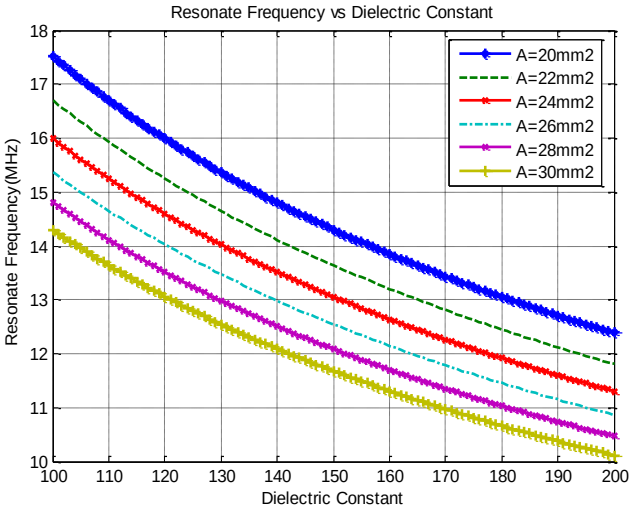

(e) Coil: N=1, R=25mm; thickness t=35um

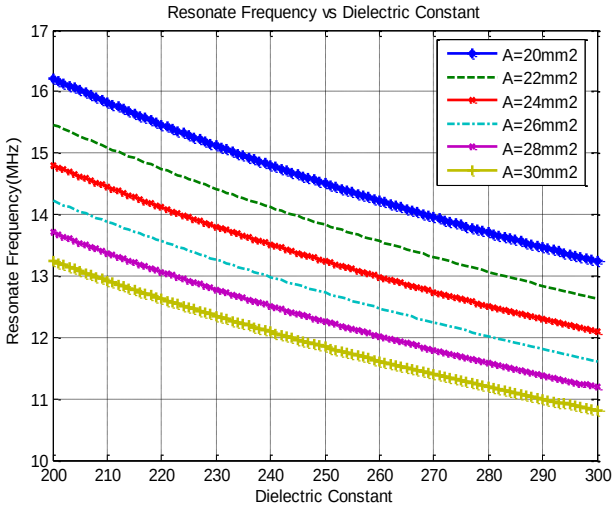

(f) Coil: N=1, R=25mm; thickness t=60 um

Figure 3. Operating frequencies Vs. dielectric constant and its thickness

2.5.4 Results and discussition

The inductance is in the order of several micro Henries and the number of turns in the spiral coil has greater impact on the value of inductance. For the capacitance of sensing element, the dielectric constant and thickness have larger influence for sensor design.

Computer simulation has been carried out to analysis inductance and capacitance and operating frequency. The relationship between sensor performance parameters: capacitance, inductance and operating frequency, and sensor geometric parameters were illustrated in a wide range for possible sensor design.

With given dielectric constant and thickness of sensing material, sensor design for a desired center operating frequency can be achieved by changing the diameter of sensor and sensing area.

In this report a battery-free wireless pressure sensor is presented with design of two major parts: a interdigital capacitor (IDC) that serves as a pressure sensing element and an inductor which works as a passive power source and data communication element. These two

components work together as an LC resonator to realize the wireless pressure sensing and remote power to eliminate the need for wire connection in conventional pressure sensor. The sensing element is comprised of a set of linear parallel electrodes coated with Polyvinylidene Fluoride (PVDF) pressure sensing material on the top. The change of capacitance in the IDC is a function of the geometry of the electrodes and the electric properties of the sensitive layer. . The sensor prototype has been made and experiment demostrated that the sensor protoype performs well in arange of 0 psi to 60 psi with an average pressure sensitivity of 25KHz/psi.

2.6 High Temperature Sensing Materials

Crucial to the success of the proposed wireless temperature sensor development is to prepare the high temperature capacitive sensing materials, which could provide large and stable temperature-dependent dielectric constant change. Intensive literature review of high temperature sensing materials was conducted. Two groups of potential candidate materials, high temperature ceramic materials and piezoelectric materials, were evaluated and discussed in terms of their dielectric and mechanical prosperities. Lead Nb Zirconate Titanate (PNZT) has been selected and prepared for the high temperature sensing. The characterization results of the PNZT high temperature sensing material demonstrated the feasibility by using PNZT to develop the proposed wireless sensor for harsh environment applications up to 350 ℃.

2.6.1 Technical approach

The temperature dependence of the dielectric constant obeys the well known Curie-Weiss law:

$$\varepsilon_r = \frac{C}{T - T_c} \tag{1}$$

Here ε_r corresponds to the relative magnetic susceptibility, C indicates a material-specific Curie constant. T means absolute temperature and T_c is the Curie temperature. Both are measured in Kelvin. According to Curie-Weiss law and the proposed capacitive temperature sensing design, the preferred material for temperature sensing is what displays the largest change in dielectric constant with temperature, which is given by:

$$\frac{d\varepsilon_r}{dt} = \frac{-C}{(T - T_c)^2} \tag{2}$$

So at a given temperature, the material with the largest dielectric constant temperature dependence is the material with the largest Curie constant, *C.* Vice versa, the material with the largest Curie constant will also display the largest peak dielectric constant value. Thus, by comparing peak dielectric constant values as well as Curie temperature in the literature, a high temperature sensitive material candidate can be determinate. In the report, high temperature ceramic materials and piezoelectric materials are discussed.

2.6.2 High temperature ceramic materials

Dielectric ceramics are electrical insulators with dielectric strength, dielectric constant and loss tangent values tailored for specific device or circuit applications. Generally, the dielectric constant of the ceramics is a function of temperature being exposed. Therefore, the dielectric

ceramic materials can be also incorporated into the capacitive sensing element for sensor applications. The following sections will provide four commonly used high temperature ceramic materials, including Beryllium Oxide (*BeO*), Aluminum Nitride (*AlN*), Alumina (Al_2O_3) and Macor, and their temperature dependent dielectric constant.

Beryllium Oxide (BeO)

There are many applications that exploit beryllium oxide (*BeO*)'s excellent electrical insulating properties, high mechanical strength, high thermal conductivity as well as good dielectric properties. Figure 1shows its dielectric constant vs. temperature variation. However, the temperature dependent dielectric constant of *BeO* is small. In addition, beryllium oxide powders are toxic when inhaled or ingested and the cost of *BeO* is kind of high. For example, one price of commercial *BeO* of *25mm x 25mm x 1.5 mm* size will cost more than $ 300.00.

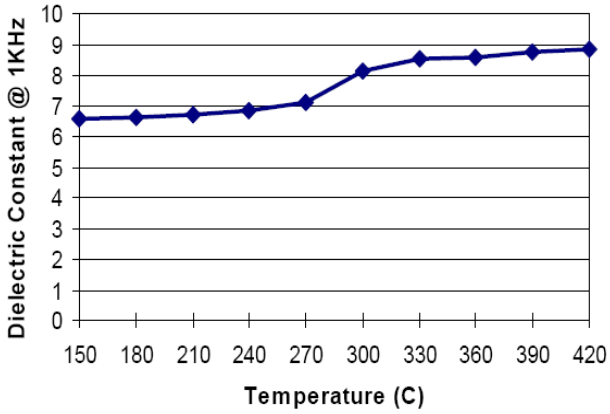

Figure 1. Dielectric constant *vs.* temperature of *BeO*

Aluminum Nitride

The dielectric properties of Alumina Nitride is shown in Figure 2. Its high thermal conductivity and better heat dissipation simplify thermal design and significantly improves circuit life and reliability. Aluminum nitride substrates have long been known to be safer to handle and have lower cost than beryllium oxide (BeO). The main drawback of AlN is its potential reactivity with water vapor in high temperature and moist environments.

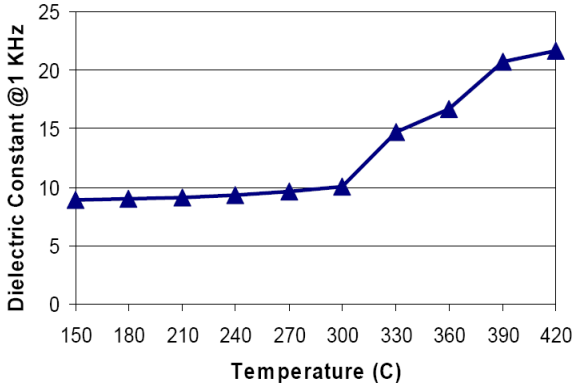

Figure 2. Dielectric constant *vs.* temperature of *AlN*

Alumina

Alumina or Aluminum Oxide (Al_2O_3) is another high temperature ceramic material candidate. Its dielectric constant changing with temperature is shown in Figure 3 at 10 kHz. Although its thermal conductivity is not as high as *BeO*, the high volume resistivity, chemical stability at aggressive and high temperature environments, high dielectric constant coupled with low dielectric loss and excellent electrical insulation lead to its wide applications in electronics as substrates. Moreover, its cost is much lower than *BeO*.

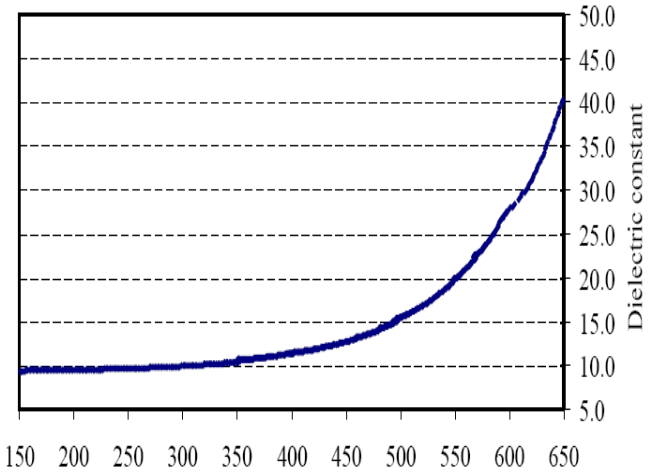

Figure 3. Dielectric constant *vs.* temperature of Alumina

Macor

Macor has very good temperature dependent dielectric change in the range from 250 ℃ to 500 ℃ at 100 kHz, as illustrated in Figure 4. Macor is an outstanding engineering material, having a continuous use temperature of 800 ℃. Fabrication of Macor is easy and fast because it can be machined into complicated shapes and precision parts with ordinary metal working tools, quickly and inexpensively, and it requires no post firing after machining.

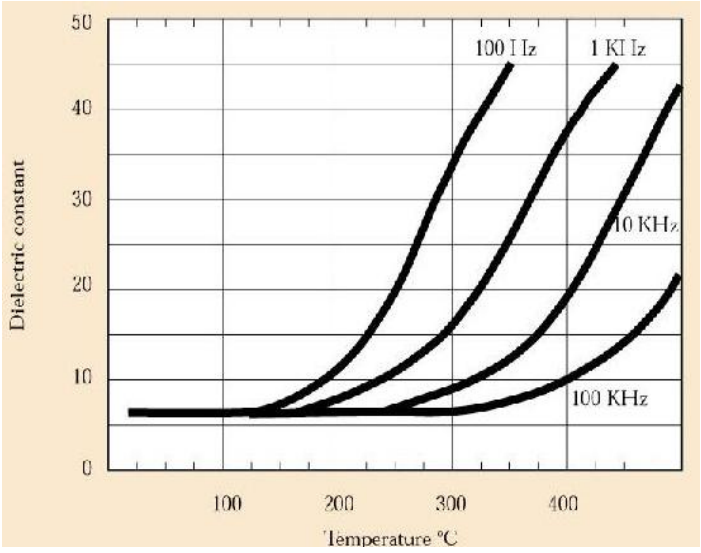

Figure 4. Dielectric constant *vs.* temperature of Macor

2.6.3 Piezoelectric Materials

Piezoelectric materials are historically utilized widely for strain gages, accelerometers and sonar based on direct piezoelectric effect and converse piezoelectric effect. However, the piezoelectric materials also have pyroelectric effect, in which the piezoelectric material responds to changes in temperature by producing an electrical response. This electrical response will influence the dielectric constant variation in changing temperature environments. Four piezoelectric materials in this group are studied.

Lead Zirconate Titanate (PZT)

The dielectric constant of PZT thin films versus temperature is illustrated in Figure 5 from room temperature to 440 ℃, as shown. The maximum dielectric constant is found at 375 ℃, close to the Curie temperature *(T_c)*, 380 ℃, of *PZT*. Below the transition temperature T_c, the dielectric constant increases quickly with temperature. Above T_c, values start to fall but increase again after further heating.

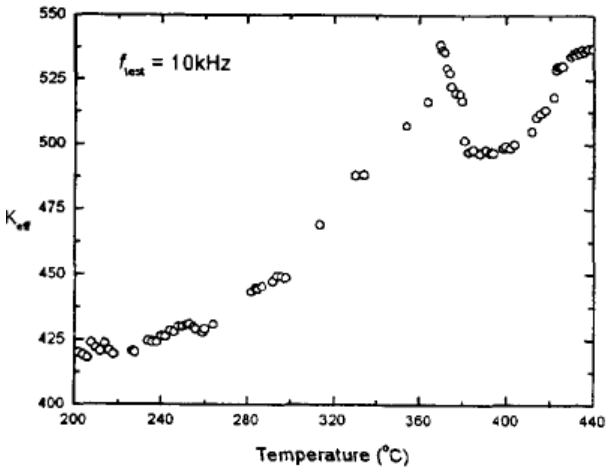

Figure 5. Dielectric constant *vs.* temperature of *PZT*

Lead Lanthanum Zirconate Titanate (PLZT)

PLZT is a transparent ferroelectric ceramic formed by doping La^{3+} ions on the A sites of (PZT). The electric applications of PLZT ceramics depends on the composition. Figure 6 shows the dielectric properties of ceramic powders PLZT 10/65/35, as a function of temperature.

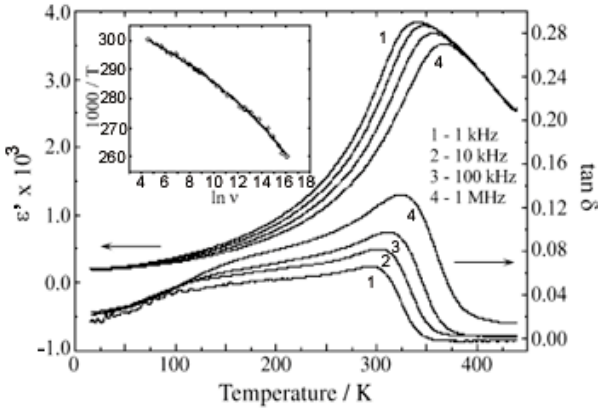

Figure 6. Dielectric constant vs. temperature of PLZT

Lead Nb Zirconate Titanate (PNZT)

Niobium modified lead zirconate titanate (PNZT) materials are formed by adding *Nb* to a *PZT* composition. The *Nb* addition enhances domain reorientation resulting in square hysteresis loops, higher coupling factors and reduced aging. The dielectric constant and loss tangent variation along with temperature is shown in Figure 7.

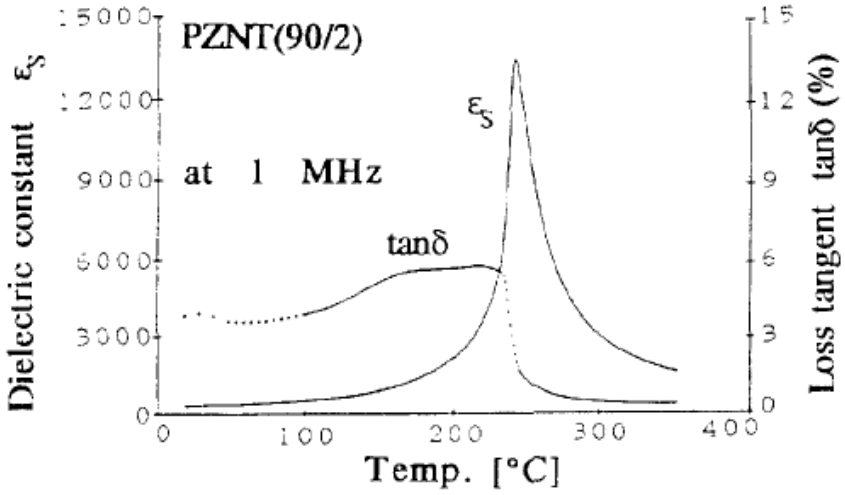

Figure 7. Dielectric constant vs. temperature of PNZT

Lead Bi Lanthanum ZirconateTtitanate (PLBZT)

Polycrystalline samples of bismuth *(Bi)* doped lead lanthanum zirconate titanate (*PLZT*) near the morphotropic phase boundary *(MPB)* are synthesized by a solid solution mixing technique. Studies of dielectric constant were obtained as a function of temperature from room temperature to 350 ℃) at 10 kHz, as illustrated in Figure 8.

.

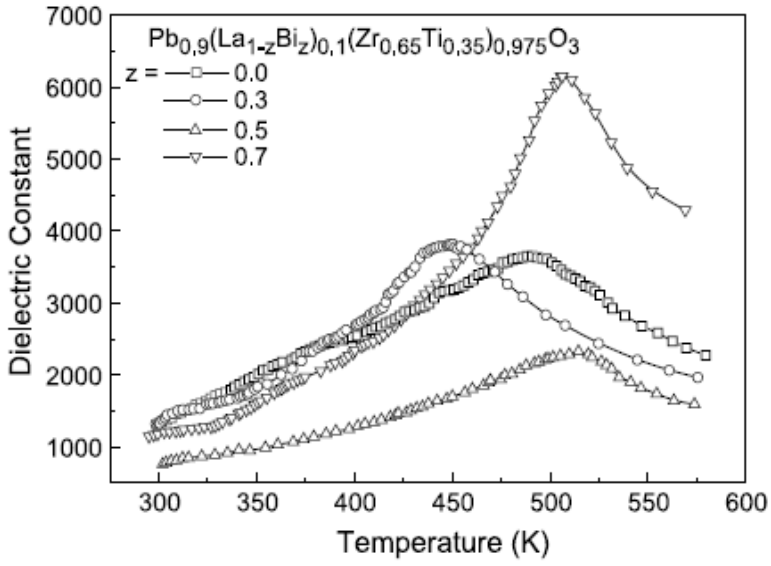

Figure 8. Dielectric constant *vs.* temperature of *PLBZT*

2.6.4 Material selection and characterization

Piezoelectric materials based on high-k ceramic dielectrics offer the best pyroelectric effect, high sensitiveness and provide large and stable temperature dependent dielectric constant changes. In comparison with temperature dependant dielectric constants and Curie temperatures among those sensing materials above, PNZT has the largest dielectric constant temperature dependence and the largest Curie constant and was selected as candidate materials for high temperature sensing. Figure 9 shows a sample of PNZT high temperature sensing material.

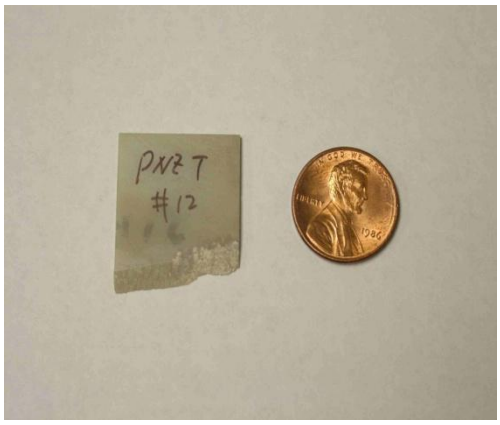

Figure 9. A sample of PNZT high temperature sensing material

The PNZT material was cut into pieces with size of 5 mm x 5 mm and coated with nickel electrodes on both sides to form capacitive sensing element.

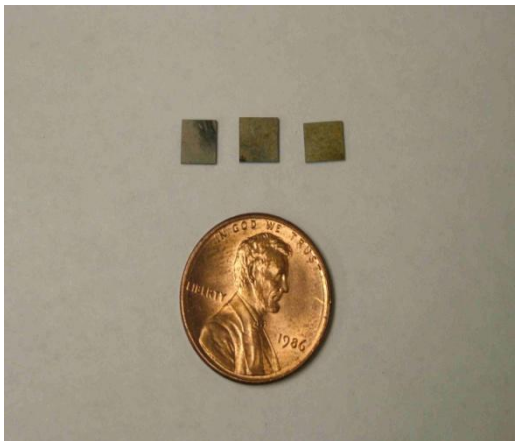

Figure 10. Samples of PNZT High Temperature Sensing Element

Dielectric constants were measured by using a RLC measurement station. The samples were placed in a high temperature oven with accurate temperature reading. Characterization result of PNZT material is show in Figure 11.

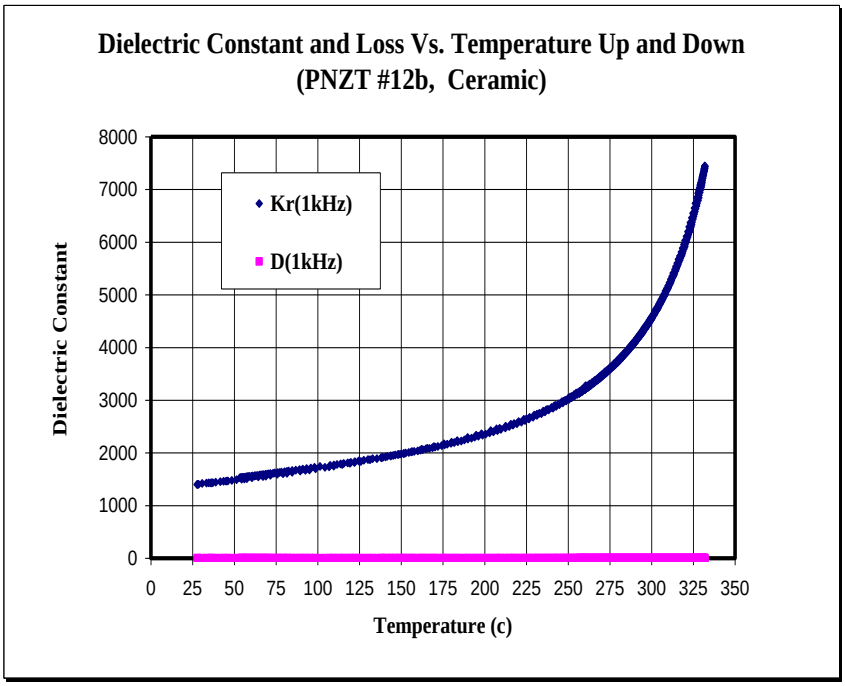

Figure 11. Characterization of PNZT High Temperature Sensing Material

2.6.5 Results and discussions

Among those reviewed eight high temperature sensing materials, PNZT shows a great promise to be employed for the proposed passive wireless temperature development based on its largest dielectric constant temperature dependence and the largest Curie constant. The characterization result of the selected PNZ, as shown in Figure 11, clearly demonstrates its dielectric constant change with temperature variation from 25 ℃ to 350 ℃ and little hysteresis was observed as the temperature was heated up and cooled down.

Lead Nb Zirconate Titanate (PNZT) has been selected and prepared for the high temperature sensing. The characterization results of the PNZT high temperature sensing material demonstrated the feasibility by using PNZT to develop the proposed wireless sensor for harsh environment applications up to 350 ℃.

2.7 Passive wireless temperature sensor design

The research during reporting period was focusing on prototype temperature sensor fabrication and characterization. This report summarizes the development of the proposed temperature sensor. Meanwhile, the preparation of the pressure sensor fabrication and characterization is also done as well.

A novel passive wireless temperature sensor, suitable for working in harsh environments for high temperature rotating component monitoring, is fabricated and calibrated. A completely passive *LC* resonant telemetry scheme, relying on a frequency variation output, which has been applied successfully in pressure, humidity and chemical measurement, is integrated with a unique high-k temperature sensitive ceramic material, in order to measure the temperatures without contacts, active elements, or power supplies within the sensor. In this paper, the high temperature sensor design and performance analysis are conducted based on mechanical and electrical modeling, in order to maximize sensing

distance, *Q* factor and sensitivity. In the end, the sensor prototype is fabricated and calibrated successfully up to 235 ℃, so that the concept of temperature sensing through passive wireless communication is proved.

2.7.1 Sensor Design and Simulation

The wireless interrogation and remote powering is achieved through an inductively powered system which generates a time varying electromagnetic field based on Faraday's law of induction and Lenz's law. As shown in Figure 1, the temperature sensor is powered by a remote reader which sends out an oscillating magnetic field by an inductive link between the reader's antenna and the sensor's inductor. At the same time, the temperature information in terms of a resonant frequency is also transmitted to the reader side through this inductive link. Because the resonant frequency of the remote reader changes when the capacitance of the sensor changes in response to environmental variables "temperature", the remote reader can detect frequency variations in the sensor's response by monitoring the impedance across the terminals of the wide bandwidth reader antenna.

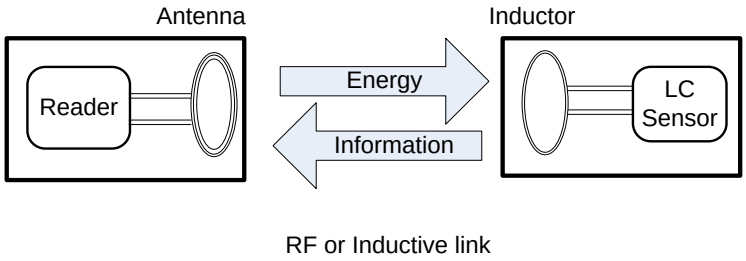

Figure 1. Basic Schematic of the Wireless Communication Proposed.

The temperature sensor, as demonstrated in Figure 2, is composed of a ceramic multi-layer capacitor integrated with planar inductor, which forms an *LC* resonant circuit. This planar capacitor structural design, incorporating with thick film high-k temperature sensitive ceramic material and thick film electrode, makes the sensor easy to attach and can be used on round rotating components, like bearings in the aircraft engine.

Electrical Capacitance (*EC*) is the basic design principle of this temperature sensor. The capacitance of the sensor is a function of the dielectric constant of the sensitive material. The planar capacitor, when exposed to harsh environments, has a linear dielectric constant variation with the temperature. The capacitance changes in response to temperature can be expressed in equation (1).

$$C_S(T) = \frac{\varepsilon_0 \varepsilon_r(T) A}{t} \tag{1}$$

Here ε_0 is the permittivity of free space of 8.85 x 10^{-12} *F/m* and ε_r corresponds to the relative dielectric constant of the dielectric material. *A* indicates the area of the electrode plate, and *t* is the distance between the electrode plates, which is also the thickness of dielectric material. Once the sensor is exposed to changing temperatures, a dielectric constant variation in the material $\varepsilon_r(T)$ will occur.

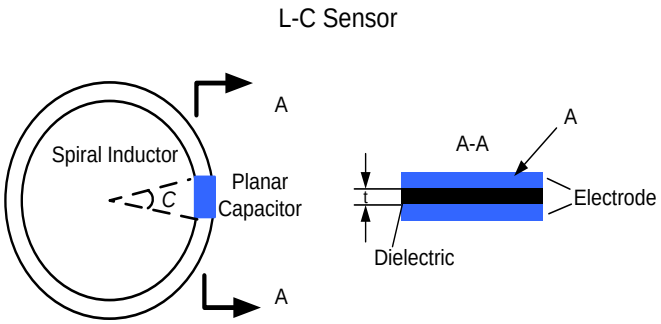

Figure 2. Schematic Diagram of Sensor Design.

The spiral inductor, as illustrated in Figure 3, constitutes a *LC* resonant circuit element for the temperature sensor, which provides a high quality factor element, feasible in harsh environment applications. Coupling the primary reader antennal (in Figure 1), the spiral inductor acts as a transformer based on the principle of electromagnetic induction. When an oscillating current is executed on the reader antenna, a changing magnetic field to both the primary and sensor inductor is produced along the magnetic path in the air. An alternating voltage of the same frequency is induced in the sensor inductor. The environmental temperature variations induce the frequency change, which can be detected from reader side by monitoring the impedance across the terminals of the wide bandwidth reader antenna. In other words, the electrical energy is transferred from the input coil to the sensor and at the same time, the temperature information is detected from the reader across the coupled magnetic field.

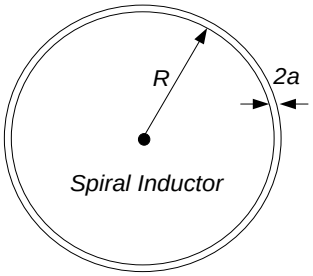

Figure 3. **Spiral Inductor Design.**

In order to read out the temperature information, it is necessary to design and fabricate an appropriate inductor to have both a reasonable inductance and a quality factor at high temperatures. Actually, there is no closed-form solution for the inductance of circular spiral inductors. The self-inductance of a circular loop of round wire (in Figure 3) has a low frequency inductance that can be estimated by [17]:

$$L_s \approx n^2 \mu_0 R \left[\ln\left(\frac{8R}{a}\right) - 1.75 \right] \quad (2)$$

Here n means the inductor turns, R indicates the loop radius, a corresponds to the wire radius, and the magnetic permeability of free space μ_0 is $4\pi \times 10^{-7}$ *H/m*.

The resonant frequency of the sensor indicates the point where a sudden change appears in the frequency response of the impedance. The expression of the resonant frequency is defined

by the following equation:

$$f_r(T) = \frac{1}{2\pi\sqrt{L_s C_s(T)}} \tag{3}$$

The simulation has been performed to present a general idea of relationship between the resonant frequency and dielectric constant, as illustrated in Figure 4, for a sensing area of electrode plate, *A*, ranging from *10 mm*^{2} to *25 mm*^{2}, a thickness of the sensitive material, *t*, of *0.480 mm*, a wire radius, *a*, of *0.337 mm*, an inductor radius, *R*, of *8.5 mm*, and turns of the inductor, *n*, of *2*.

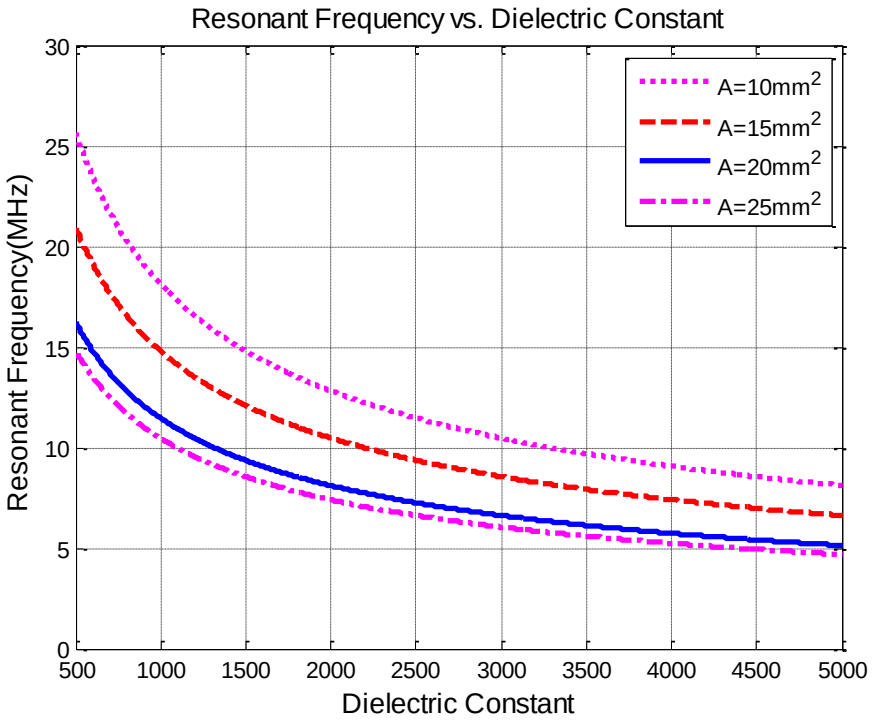

Figure 4. the Frequency *vs*. Dielectric Constant.

2.7.2 Performance Analysis: Electrical Model

The classical approach to analyze the wireless sensor system is to eliminate the coupled reader coil and the sensor by reflecting impedances back to the reader, in order to clarify the voltage change of reader coil. The equivalent circuit diagram is shown in Figure 5. Here, Z_R and Z_S indicates the inherent impedances from the reader and sensor respectively, R_R and R_S are the self resistances of the reader and the sensor circuit, C_R is the capacitance of the reader circuit, which is introduced in order to maximize the current applied through the reader antenna, C_S is the sensor capacitance, which is sensitive to environment temperature. Z_s' is the reflected impedance of the sensor, Z_i is the input impedance seen from the reader side, and *M* corresponds to the mutual inductance.

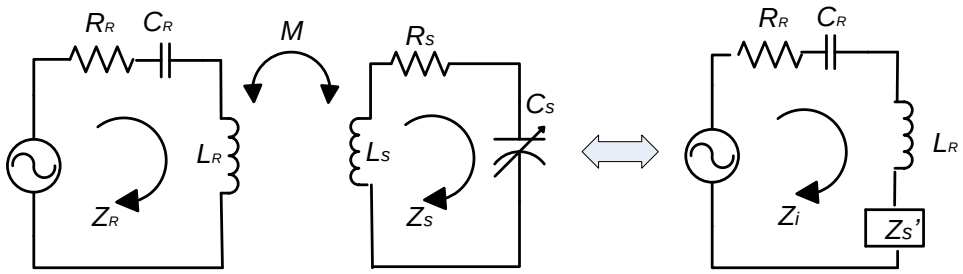

Figure 5. Equivalent Circuit Diagram of Wireless Telemetry System.

The impedance of the resonant circuit of the reader is given by:

$$Z_R = j\omega L_R + R_R + \frac{1}{j\omega C_R} \tag{4}$$

The impedance of the sensor side can be expressed as:

$$Z_S' = \frac{(\omega M)^2}{j\omega L_S + R_S + \frac{1}{j\omega C_S}} = -\frac{\omega^2 k^2 L_R L_S}{j\omega L_S + R_S + \frac{1}{j\omega C_S}} \tag{5}$$

Here *k* is the coupling coefficient, defined by:

$$k = \frac{M}{\sqrt{L_R L_S}} \tag{6}$$

In fact, the sensor interaction can be seen as a load $\Delta Zs'$ placed in series with the inductance antenna:

$$\Delta Z_S' = \frac{\omega^2 k^2 L_R L_S}{j\omega L_S + R_S + \frac{1}{j\omega (C_S + \Delta C_S)}} \tag{7}$$

Therefore, the input impedance seen from the reader side is given by

$$Z_i = Z_R + Z_S' \tag{8}$$

Substitute (4) and (7) into (8), it will yield:

$$Z_i = j\omega L_R + R_R + \frac{1}{j\omega C_R} + \frac{\omega^2 k^2 L_R L_S}{j\omega L_S + R_S + \frac{1}{j\omega (C_S + \Delta C_S)}} \tag{9}$$

A voltage drop caused by the sensor side circuit is treated as the reflected impedance Z_S' multiplied by the current. Actually, instead of measuring the voltage change at a certain frequency, a periodical sweeping frequency around the sensor's natural frequency is generated to measure a frequency variation. As the reader's frequency is swept, once the excitation frequency matches to the resonant frequency from the sensor side, a sudden increase in the sensor impedance Z_S' occurs. Figure 6 shows the magnitude of impedance and phase of this reflected sensor impedance Z_S' verse the sweeping frequency changes at different temperatures, with the parameter values summarized in Table 1.

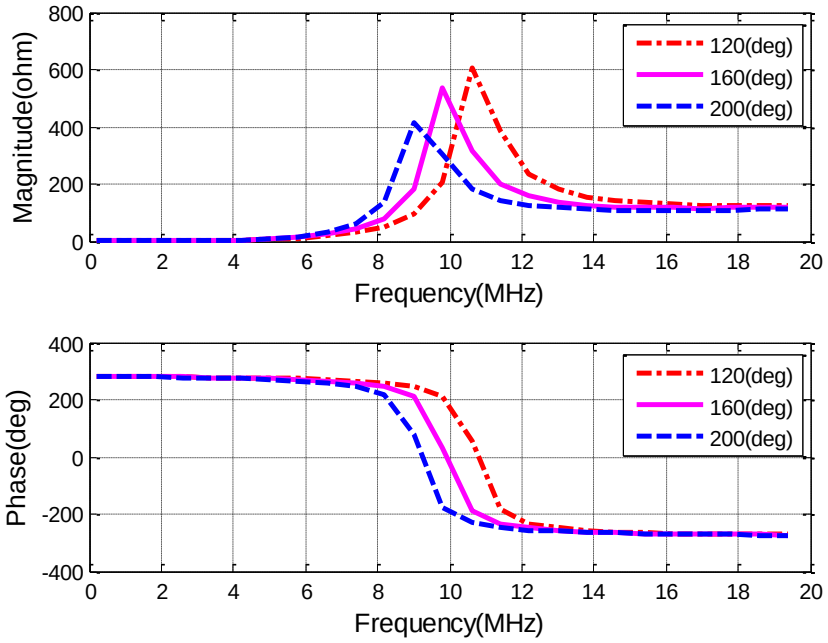

Figure 6. Input Impedance *vs*. Sweeping Frequency.

In order to be able to detect the resonant frequency from the reader's side, the variation of the reflected impedance, *Zs',* should be high enough. If the changes of reflected impedance from the sensor, *Zs',* are smaller than those of inductance from the antenna, most of the voltage drop will occur across the antenna. This will bury the change of reflected impedance *Zs'* caused by the remote sensor. For this reason, the *Q*-factor and coupling coefficient should be high enough to make sure that the resonant frequency can be detected.

Table 1 System Parameter Values

Reader Inductance L_R	1.5 μH
Sensor Inductance L_S	0.68 μH

Sensor Total Resistance R_L	6 ohm
Sensor Nominal Capacitance C_S at 20 ℃	0.24 nF
Nominal Coupling Factor k	0.4
Reader Radius r_R	30cm
Inductor Radius r_S	28.5cm
Coupling Distance d	2.5cm

2.7.3 Performance Analysis : Q-factor

The quality factor, Q, is defined as the ratio of total stored energy to dissipated energy per unit cycle of the resonant system:

$$Q = \frac{W_{total}}{P / 2\pi f} = \frac{2\pi f W_{total}}{P} \tag{10}$$

where W corresponds to the total stored energy, P indicates the average dissipated power, and f is the resonant frequency. There is another expression of Q-factor defined as follow:

$$Q = \frac{2\pi f_r L_S}{R_L} = \frac{1}{R_L}\sqrt{\frac{L_S}{C_S}} \tag{11}$$

where R_L is the total sensor resistance consisting of the inductor resistance, capacitor resistance and circuit resistance, which is briefly discussed by Musunuri et. al. in [18].

Qualitatively, the Q-factor is generally interpreted as an indication of the sharpness of the resonance peak. A higher Q-factor indicates a lower rate of energy dissipation relative to the oscillation frequency. Figure 7 presents the simulation of the Q-factor verses total sensor resistance and sensor inductance, where the same nominal values of other parameters in Table 1 are used.

2.7.4 Performance Analysis: *Coupling Factor*

The coupling coefficient k is the factor dominating the wireless range of inductive telemetry systems. For a complete system description, k can be modeled and optimized specifically for each application by using finite element *CAD* tools and models. However, a fair approximation of k related to design parameters is given by [19]:

$$k(d) = \left(\frac{r_S r_R}{d^2 + r^2}\right)^{\frac{3}{2}} \tag{11}$$

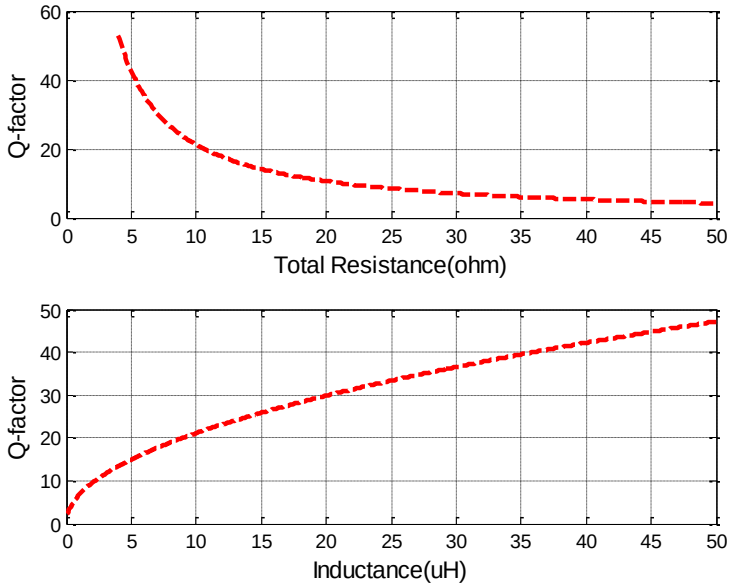

Figure 7. Q-factor *vs*. Resistance & Inductance.

Here r_R corresponds to the radius of the primary coil, r_S indicates the radius of the sensor inductor, and d means the coupling distance. Figure 9 presents how the reader antenna radius and the radius ratio of the sensor radius and the reader antenna affect the coupling factor k at a certain communication distance (parameters used are shown in Table.1) The simulation indicates that minimizing the antenna radius and maximizing the radius ratio will improve the coupling factor and maximize the coupling distance.

2.7.5 Results and discussions

In this section, the performance investigation of the passive wireless temperature sensor is conducted with respect to resonant frequency, *Q*-factor and coupling factor. In addition to the parameters adjustment mentioned above, capacitance compensation can also be adopted to maximize reflected sensor impedance in order to make the resonant frequency detectable, that is, introducing a capacitance into the reader's side to make another resonant circuit, leaving the full sensor impedance change expressed at the reader's side. However, this capacitor would be able to change according to the resonant frequency value for maximum efficiency, which may not be easily accessible. This would also require more sophisticated compensation architectures.

All in all, improvements are concluded as follows in order to achieve high performance wireless system, characterized with a high *Q*-factor and a maximized communication distance:

to maximize sensor inductance, the radius ratio of the sensor inductor and reader coil;

to minimize the sensor resistance, the radius of the reader antenna, reader inductance;

to introduce reader capacitance compensation.

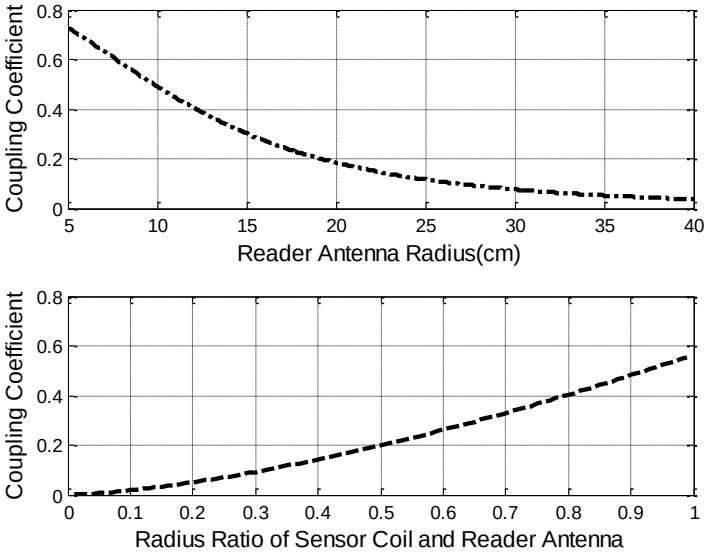

Figure 8. Coupling Coefficient *vs.* Reader Antenna Radius & Radius Ratio.

2.8 Sensor fabrication and calibration

The sensor prototype and its equivalent circuit are shown in Figure 9. The spiral inductor with two turns is made of enamel-coated magnet copper wire, connected to the electrodes of the capacitor by *6041D* Ag. The diameter of the round copper wire *2a* is *0.674 mm*; the radius of the inductor *R* is *28.5 mm.* The area of the electrode plate *A* is *25mm*^{2} and the thickness of dielectric material *t* is *0.480 mm*. Here, L_S indicates the sensor inductance, C_S means the sensor capacitor, R_S corresponds to the ohmic resistance in the sensor and Z_S demonstrates the impedance of this sensor prototype.

Figure 9. the Sensor Prototype and Equivalent Circuit.

Figure 10 demonstrates the principle of sensor calibration experiment. The temperature sensor is deposed into a glass of oil, which is heated using Hot Plat, providing the temperature range from room temperature to 400 ºC. The oil's temperature is measured by thermometers directly. At the same time, the antenna of the reader is laid outside of the glass jar, which transfers the temperature information to the reader. This information can be read out from Oscilloscope in terms of Resonant Frequency. Moreover, the *DAQ* card can also acquire the temperature variation information in real-time and then be read out from laptop using *Matlab* data acquisition toolbox.

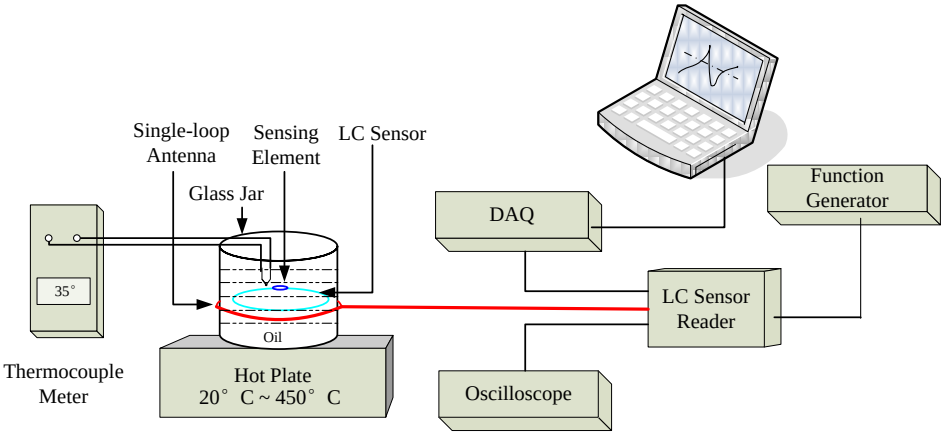

Figure 10. Principle of the Sensor Calibration Experiment.

When the sweep frequency is generated by the Function Generator, the resonant frequency would be monitored by the Oscilloscope or read out by Laptop. Resonant frequency variations are recorded along with temperature variations. The calibration result is plotted in Figure 11. This result proves that the *LC* temperature sensor made of this high-k ferroelectric material is feasible in wireless temperature monitoring. The ferroelectric material of the capacitor is responsive to environment temperature. This demonstrates that the capacitance is sensitive to temperature variations and then the resonant frequency is responsive to environmental temperatures.

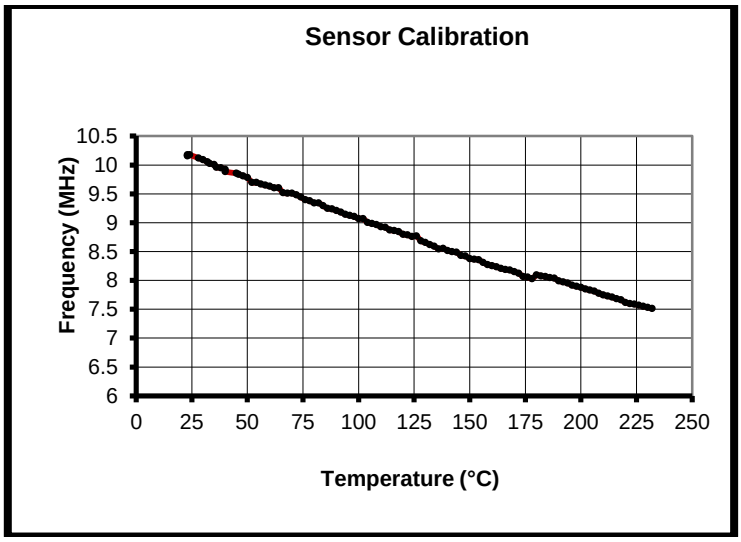

Figure 11. Sensor Calibration.

This result presents the development of a novel passive wireless temperature sensor, capable of operating in harsh environments for high temperature rotating component monitoring. A passive *LC* resonant telemetry scheme, relying on a frequency variation output, has been integrated with the sensor, thereby eliminating the need for physical contacts, active elements, or power supplies, which cannot withstand harsh environments. This project extended the knowledge base of passive wireless temperature sensing technologies in harsh environment and advance embedded prognostics health monitoring technologies. In conclusion, in this paper, the unique high-k temperature sensitive ceramic material has been

applied instead of any electronic components to realize *LC* tank temperature sensing. A novel high-k temperature sensitive ceramic material has been developed which is able to work in harsh environment up to 235℃. Additionally, the unique temperature sensitive ceramic material has been integrated into the *LC* resonant tank circuit to create a frequency-encoded sensing mechanism which could dramatically increase sensitivity and dynamic response of the wireless temperature sensor.

2.9 Results and discussions

The proposed passive wireless temperature sensor, suitable for working in harsh environments for high temperature rotating component monitoring, is fabricated and calibrated. The first calibration result of the prototype sensor shows that the sensor is able to work in harsh environment up to 235℃. From the PNZ characterization result in last report, the sensor could operate up to 350 ℃. The reason why the calibration was stopped at 235 ℃ is because the joint between sensing element and inductive coil was broken at 235 ℃. We are working on using LTCC technology to package the sensor and eliminate joint between sensing element and inductive coil.

2.10 Application to temperature monitoring of a rotational component

The temperature sensor prototype and its equivalent circuit are shown in Figures 6a and 6b respectively. The sensor was built using a 5 mm square piece of PLZT ceramic. Two thin wires were bonded into both surfaces of the ceramic using the *Duralco 124 Ultra Temp Conductive Epoxy*, which is a electrically conductive epoxy. The piece of ceramic was entirely covered with a layer of a *Resbond 920*, which is a high thermal conductor and an excellent electrical insulating epoxy. This last coating was used to protect the bonding between the electrodes and the ceramic and to prevent the sensor from making any electrical contact with any exterior component.

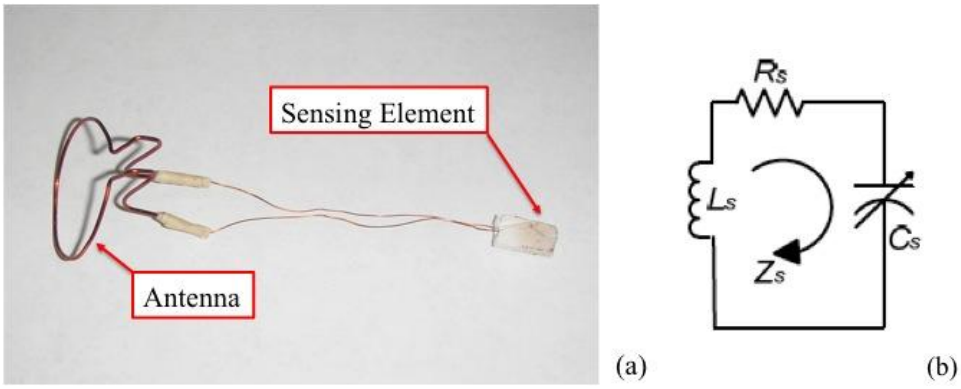

Figure 12. Wireless temperature sensor (a) and sensor equivalent circuit (b).

The sensor was attached to an aluminum disk as shown in Figure 7. A machine fault simulator from Spectra Quest was used to conduct the sensor testing. The machine was operated at a low rate of 288 rpm (4.8 Hz). Since the distance between reader and sensor antennas affects the coupling coefficient, both antennas were placed as close as possible while avoiding any physical contact. The reader antenna was placed around the fault simulator shaft and aligned concentrically with the sensor antenna at a distance of 3 mm. This wireless arrangement demonstrates the advantage of the developed sensor technology since it eliminates the need for potentially unreliable, high-temperature contacts on the sensor [6].

Before rotating, the disk was preheated to a temperature of 226°C using an electric heater. Subsequently, the machine was turned on to let the disk rotate and cool down while the temperature was registered using an infrared thermometer gun and the frequency was detected using the portable reader. A series port monitoring software was used to capture the resonant frequency and translate it into temperature information.

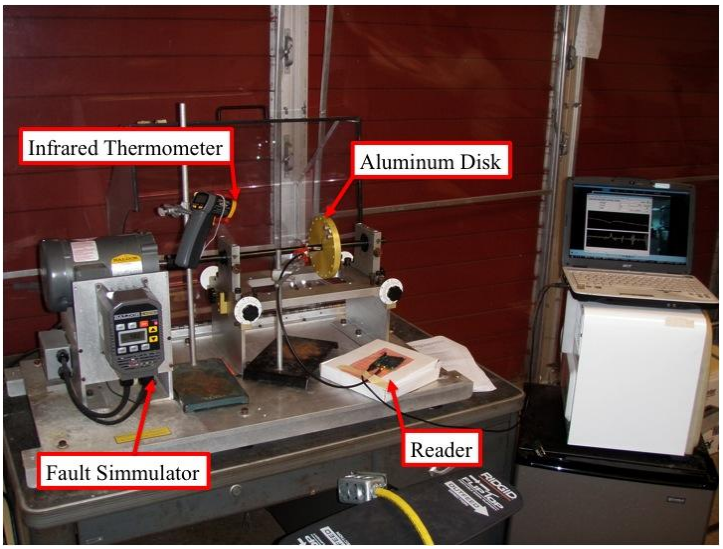

Figure 13. Experimental setup.

2.10.1 Results and Discussions

As demonstrated in the simulation presented in Section 4, a periodical sweeping frequency was generated around the sensor's natural frequency. When the reader's frequency matches the sensor's resonant frequency, a sudden increase in the sensor impedance occurs. Figure 8 shows the experimental result of impedance vs. resonant frequency in the experiment.

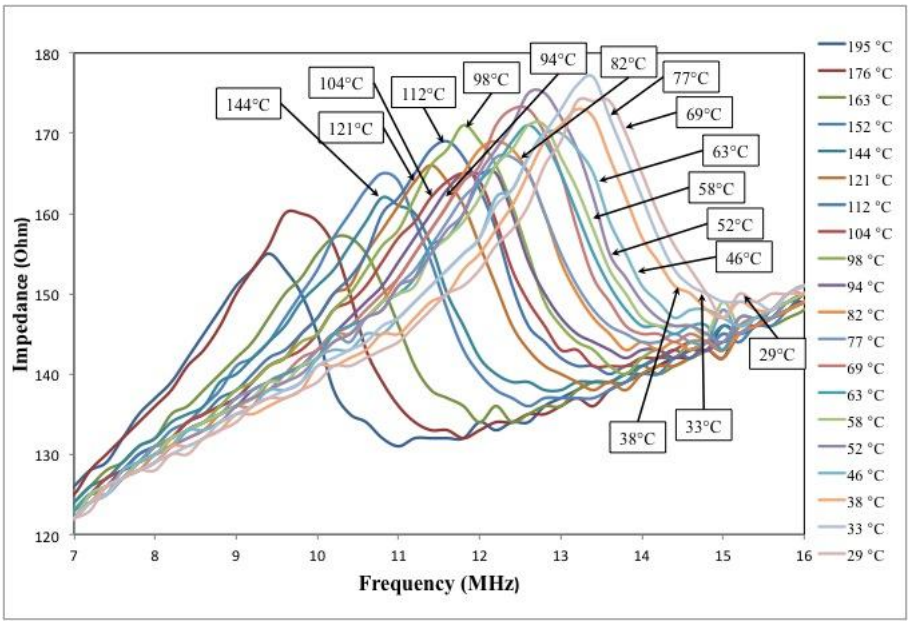

Figure 14. Sensor prototype temperature response; Sensor Impedance vs. Frequency.

Since the dielectric properties of the material are temperature dependent, a shift in the sensor's resonant frequency is produced in response to temperature changes. It is noticed that there is a linear pattern in the variation of the frequency in each of the data points. The slight magnitude difference of each peak might be due to misalignments between the centers of both inductive antennas while the disk is rotating. These misalignments may result in a decrease in the coupling factor, which is further determined by the shape of the coils and the angle between them and is dependent on the distance and their relative size [7,8]. A decrease in the coupling factor results in a decrease of the sensor impedance, reflecting peaks with lower magnitudes.

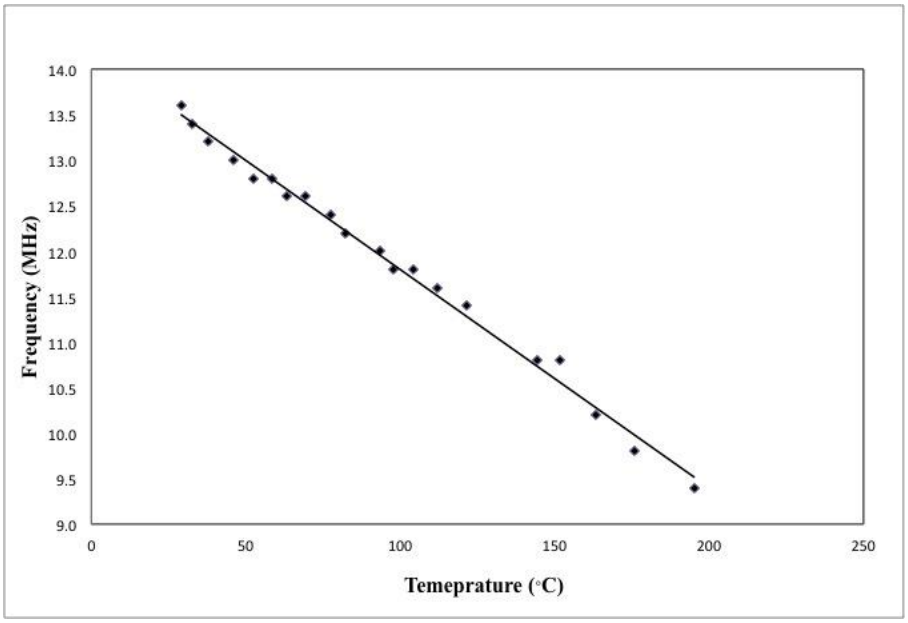

Figure 15. Frequency vs. Temperature Plot.

Figure 9 demonstrates the variation of the resonant frequency due to variations in temperature. A linear dependency of the resonant frequency on the temperature is clearly seen. As previously described in Section 3, there is a temperature dependency on the material permittivity, resulting in a change of the capacitance and a shift in the resonant frequency of the sensor. This variation can be captured wirelessly as was done in this experiment. As a result, it is demonstrated that the sensor developed in the project can be used to monitor temperature in rotating components.

2.10.2 Conclusions

This report presents the development of an innovative passive wireless temperature sensor capable of operating in rotating components and harsh environments. The design was based on a RF-powered temperature sensor consisting of a capacitive sensing element and an inductive antenna. The wireless sensor developed for temperature sensing in this study is based on principle of near-field sensing technology and was realized by employing an inductor-capacitor (L-C) tuned electronic oscillator incorporated with temperature sensitive materials. The uniqueness of this device resides in the integration of a temperature sensitive material (PLZT) into the LC tank to measure temperature in rotating components. The sensor operated in harsh environments above the 200°C and captured the signal while attached to a rotating

component. This demonstrates the feasibility and concept of a passive wireless temperature sensor interrogating system for rotating components. In order to use this device in a harsh operating environment, as is the case of compressor and turbines, more research must be done to develop a final commercial design. A design for a harsh operating environment will require research in temperature sensitive materials and packaging technologies.

The temperature sensing technology presented in this report has many advantages such as being wireless and passive and possessing a simple design. Future testing will be carried out in order to optimize and extend the operating temperature range. Further research is also under way to test the effects of the rotating speed on the sensor performance. The current research demonstrates that temperature monitoring can be achieved without requiring physical contact, power supplies, or active elements in the circuit.

3. Passive Wireless Pressure Sensor

3.1 Introduction

While there has been significant progress in sensor technology for structural health monitoring, there still exists the need for a self-powered and wireless sensing system, which can be integrated into an engineered system. Existing pressure sensing technologies offer outstanding performance in terms of the resolution and time response. However, these technologies require either physical connection of signal communication, battery power supply or expensive equipments for acquiring pressure information [1, 2, 3, 4]. These limitations make existing pressure sensing technologies unsuitable for most of the structures health monitoring applications.

In this report a battery-free wireless pressure sensor is presented . The sensor consists of two major parts: a capacitor that serves as a pressure sensing element and an inductor which works as a passive power source and data communication element. These two components work together as an LC resonator to realize the wireless pressure sensing and remote power to eliminate the need for wire connection in the conventional pressure sensors. An interdigital capacitor (IDC) coated with Polyvinylidene Fluoride (PVDF) pressure sensing material on the top is used for pressure sensing and an inductor coil is adopted as antenna, The sensor prototype has been made and experiment demostrated that the sensor protoype performs well in the range of 0 psi to 60 psi with an average pressure sensitivity of 25KHz/psi.

3.2 Principle of operation

Principle of the proposed pressure wireless sensing is based on the operation of an inductor-capacitor (L-C) tuned electric oscillator. . The L-C oscillator works on the storage of energy in the form of electric charge in the capacitor and in the form of magnetic field in the inductor. The property to be sensed, such as pressure in this case, induced the variation of sensor capacitance due to electrical properity change.of the sensing material. The remote reader detected this information by monitoring resonant frequency shifts due to impedance changes in response to property change. In the L-C tank circuit, the velocity of the current flows from the capacitor to the inductor or vice versa, produces resonant frequency (F) that depends on the values of the capacitor (C) and the inductor (L), and is expressed by the equation (1) :

$$F = \frac{1}{2\pi\sqrt{LC}} \quad (1)$$

The Figure 1 shows the schematic of a battery-free passive wireless sensing system. It consists of a sensor unit, which does not have any power source of its own, and a transceiver unit, which provides energy to the sensor. The sensor provides information back to the transceiver via the inductive link.

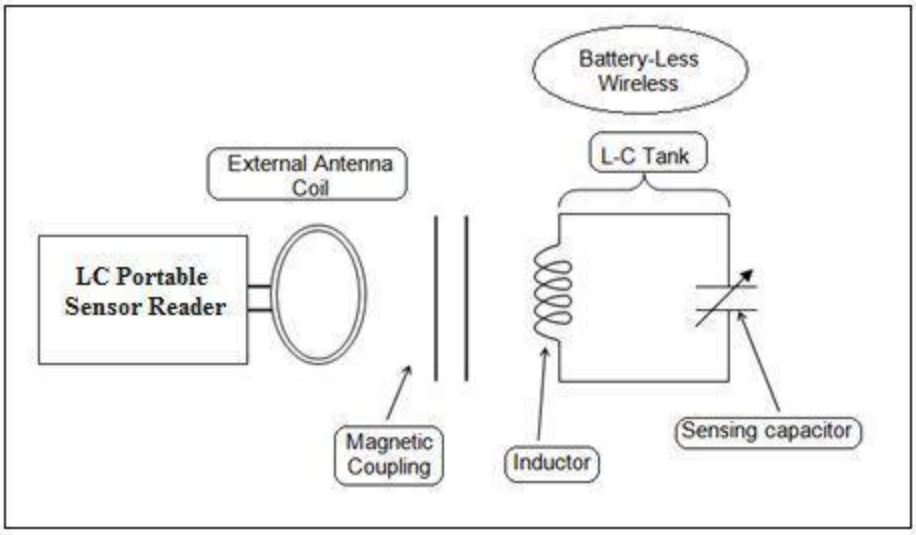

Fig. 1. Schematic of a battery-free passive wireless sensing system.

The operating principle behind the interdigital capacitor is very similar to the one observed in a parallel plate capacitor; Figure 2 shows the relationship between a parallel plate capacitor and an interdigital capacitive sensor, and how the transition occurs from the parallel plate capacitor to a interdigital capacitive sensor. There is an electric field between the positive and negative electrodes and Figure 2 a, b and c shows how these fields pass through the material under test (MUT). Thus material dielectric properties as well as the electrode and material geometry affect the capacitance and the conductance between the two electrodes.

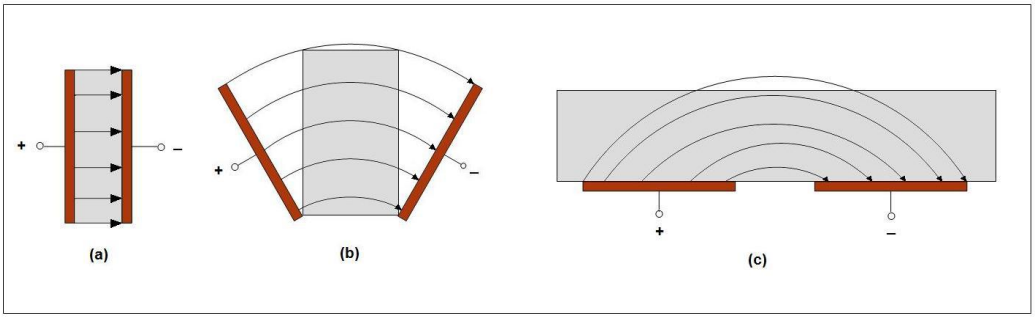

Fig. 2. Operating principle of interdigital sensor

The remote reader across inductive powering will generate a magnetic field induced by an alernating current and the proposed pressure sensors will be place within that magnetic field as shown in Figure 3. In this resonant circuit Z_R and Z_S indicates the inherent impedances from the reader and sensor respectively, R_R and R_S are the self resistances from the reader and sensor, C_R is the capacitance of the reader, which is introduced in order to maximize the current applied through the reader antenna, C_S is the sensor capacitance, which is sensitive to environment pressure, L_R and L_S indicates the inductance from reader and sensor respectively. $Z_s^{'}$ is the reflected impedance of the sensor, Z_i is the input impedance seen

from the reader side, and M corresponds to the mutual inductance [9].

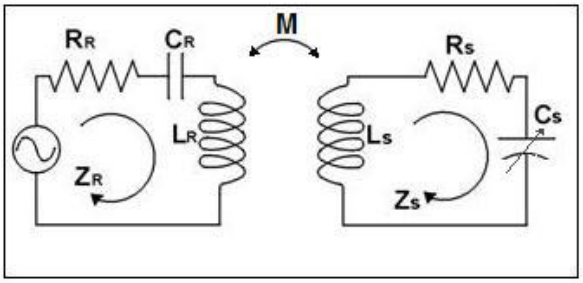

Fig. 3. Inductive Coupled Reader and LC Sensor

The equivalent circuit diagram of the resonant circuit of the reader with the inductive coupled sensor is shown in Figure 4.

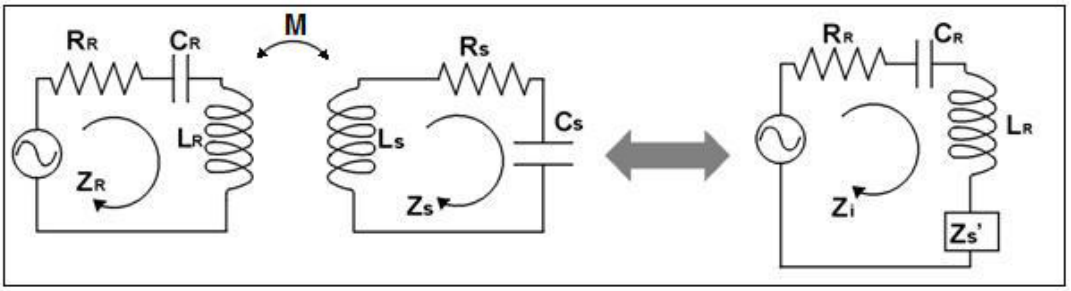

Fig. 4. Equivalent Circuit Diagram of Wireless Telemetry System

The impedance of the resonant circuit of the reader is given by:

$$Z_R = jwL_R + R_R + \frac{1}{jwC_R} \tag{2}$$

The impedance of the sensor side can be expressed as:

$$Z'_S = \frac{(wM)^2}{jwL_S + R_S + \frac{1}{jwC_S}} = -\frac{w^2k^2L_RL_S}{jwL_S + R_S + \frac{1}{jwC_S}} \tag{3}$$

where k is the coupling factor, defined by:

$$k = \frac{M}{\sqrt{L_RL_S}} \tag{4}$$

The sensor interation can be seen as a load variation $\Delta Z_{S'}$ placed in series with the inductance antenna, defined by:

$$\Delta Z_{S'} = \frac{w^2k^2L_RL_S}{jwL_S + R_S + \frac{1}{jw(C_S + \Delta C_S)}} \tag{5}$$

The input impedance seen from the reader side is defined by:

$$Z_i = Z_R + Z_{S'} \tag{6}$$

Using the equation (1) and (2) into (5), we have the input impedance seen from the reader defined by:

$$Z_i = jwL_R + R_R + \frac{1}{jwC_R} + \frac{w^2 k^2 L_R L_S}{jwL_S + R_S + \frac{1}{jw(C_S + \Delta C_S)}} \quad (7)$$

The reflected impedance $Z_{S'}$ multiplied by the current is equivalent to the voltage drop caused by the sensor side cirucuit.

In the portable reader a signal is used to generate a periodical sweep of the frequency around the sensor's resonant frequency to measure a frequency variation. A sudden increase in the sensor impedance $Z_{S'}$ occurs, when the excitation requency coincide the sensor's resonant frequency. The Figure 5 shows the magnitude of impedance of the sensor impedance $Z_{S'}$ in response to the sweeping changes, the simulation is calculated by the parameter values in table I.

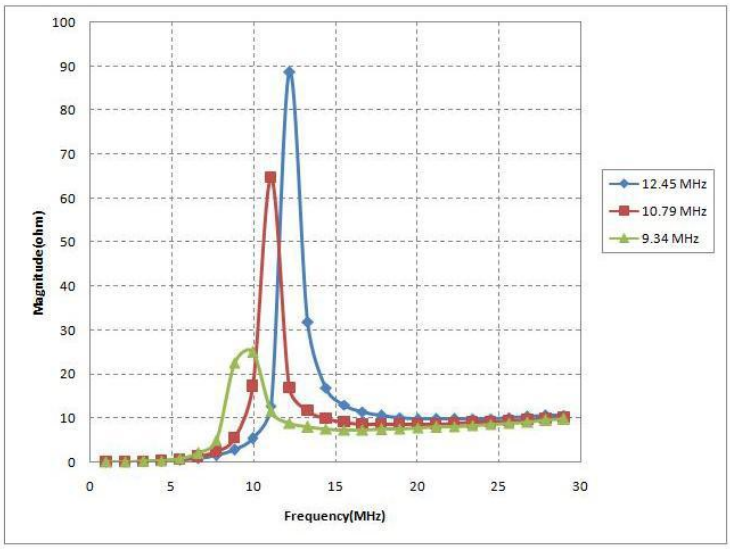

Fig. 5. Magnitude $Z_{S'}$ versus f

Table 1. Electrical Parameter Values for Interdigital sensor

PARAMETER	SYMBOL	VALUE
Sensor Nominal Capacitance	Cs	19.4 pF
Sensor Inductance	Ls	5.57 H
Resonant Frequency	fo	17.44Mhz
Sensor Resistance	Rs	0.5Ω
Reader Inductance	Lr	0.1169 µH
Reader Radius	r_R	2.5 cm
Inductor Radius	r_S	2cm
Coupling Distance	d	2cm
Nominal Coupling Factor k	k	1 cm

3.3 Sensor Modeling

The design of the sensor relies on the properties especially resonant frequency f_0 and quality

factor Q, which is a function of L_S, C_S and R_S, and the total capacitance C_S is a function of two dimensional parameters, η (metallization ratio) and r (Layer thickness to wavelength ratio), length and number of electrodes, height of sensing layer and as well as the dielectric permittivity of each layer (substrate, protective layers and sensing layer)

$$C = C(\eta, r, \varepsilon_s, \varepsilon_{PVDF}, \varepsilon_{Poly}, h_2, h_3, l, N)$$

3.3.1 Capacitance estimation

Conformal mapping is one of the most frequently used approaches to transform an appropriate space region of IDC to a parallel plate capacitor geometry whose capacitance value can be calculated. Igreja [10] developed an analytical solution for IDC capacitance using conformal mapping.

The geometric dimensions of the IDC are indicated in Figure 6, this figure shows a 2-dimensional cross-sectional view of the IDC with all the geometric dimensions and dielectric properties notified, where t is the thickness of the IDEs, h is the thickness and ε_S is the permitivity of the substrate. The gaps between electrodes have a width of g_c and the fingers have a width of w_c. All the fingers are connected to two common comb electrodes. Each comb electrode has a number of finger of length L_c and is connected to each end of the spiral inductor. The wavelength is calculated by $\lambda = 2(g_c + w_c)$. The dimensional parameter which the capacitance also depends on is called metal ratio and is calculated as $\eta = w_c/(g_c + w_c) = 2w_c/\lambda$

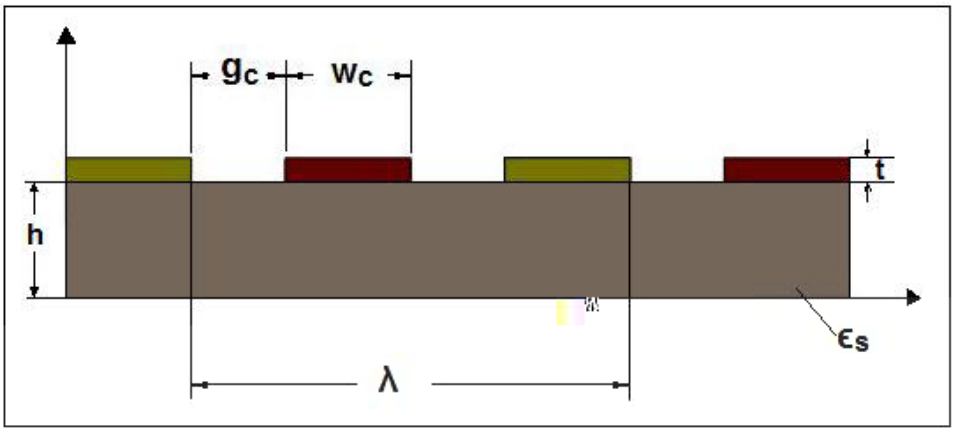

Fig. 6. Two dimensional cross-sectional view of the IDC with the geometric dimensions

The proposed battery-free interdigital pressure sensor will be mounted between to layer of polyethylene with 3mm of thickness each; avoiding the presence of metal near to the IDC. The schematic view of the IDC on the test machine is shown in the Figure 7. By symmetry, the perpendicular planes halfway between the electrodes are equipotential planes with V=0, it acts like an electric ground where electric field lines crossing normal to these planes shown in Figure 8.

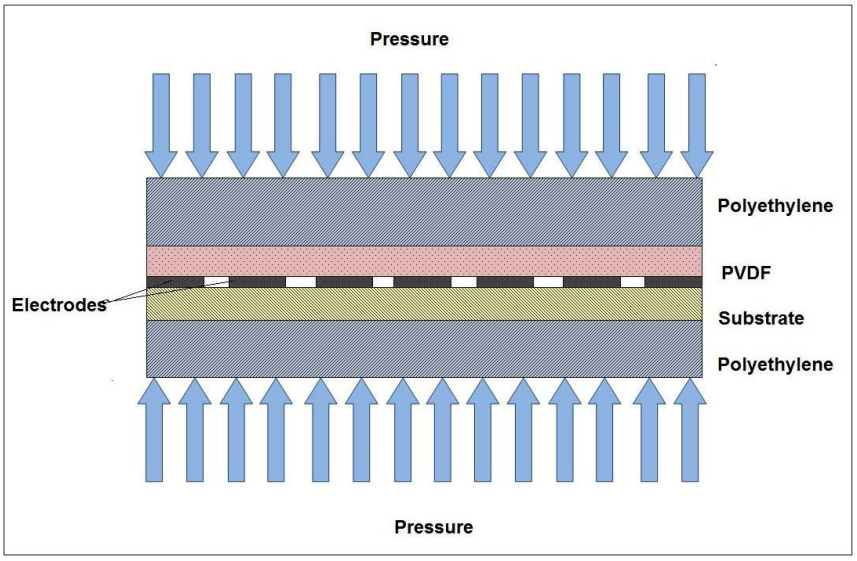

Fig. 7: Schematic view of the IDC on the test machine

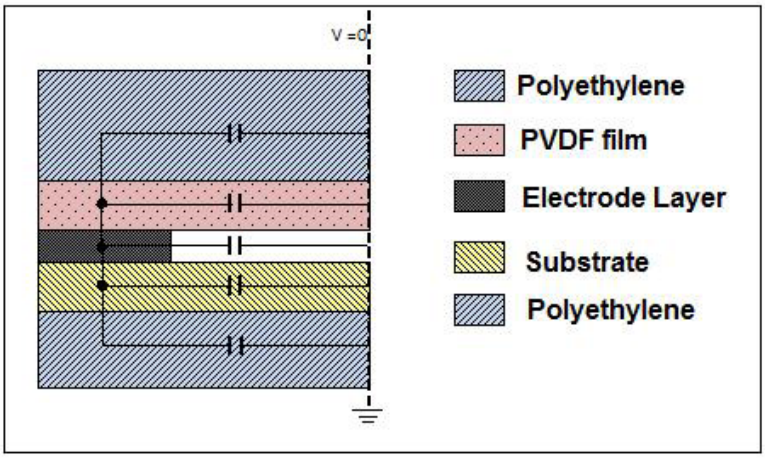

Fig. 8. A half unit cell model of the proposed multilayer IDC

The equilibrium circuit of our proposed multilayer interdigital capacitor using the model on a testing beam is shown in Figure 9. Based on the so-called partial capacitance technique, the proposed three-layered structure for the IDC pressure can be split into five individual layers with capacitances shown in Figure 10.

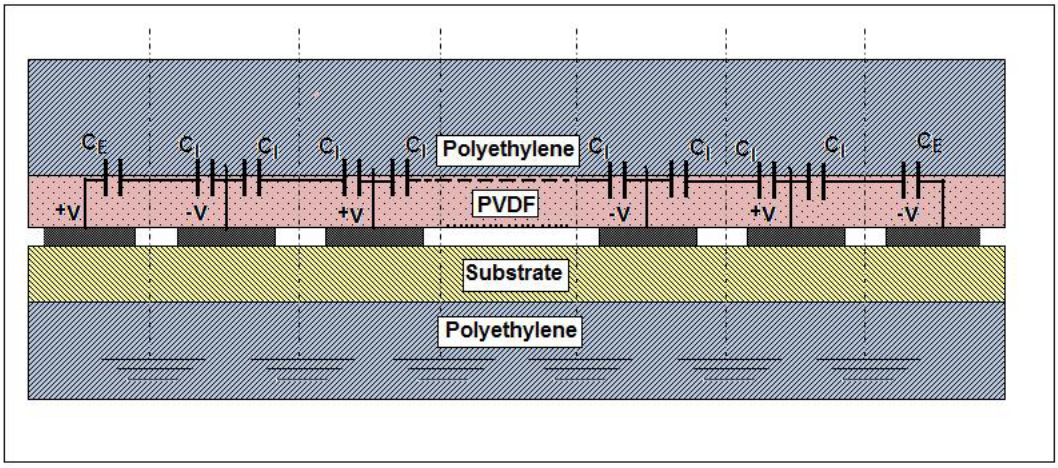

Fig. 9. The equivalent circuit of the static capacitance of a multilayer interdigital capacitor

At the lower half plane of the IDC, the thickness of the substrate ($\approx 18\,\mu m$) is not much smaller than the wavelength of the IDC so that the substrate can be considered as a finite layer. Since the thickness of the polyethylene layers ($\approx 3mm$) is much greater than the wavelength, and thus the thickness of the polyethylene layers are considered as an infinite layer. At the upper half plane, the pressure sensitive layer is considered as finite layer. The calculation of either the C_I or C_E can be done based on this half unit cell model as is shown in the Figure 8.

The total capacitance of the half unit cell C_I and C_E can be treated as a summation of four individual capacitances which are given below:

$$C_I = C_{I_{P\,oly\,\infty}} + C_{I_{PDVF}} + C_{I_{substrate}} + C_{I_{P\,oly\,\infty}} \quad (8)$$

$$C_E = C_{E_{P\,oly\,\infty}} + C_{E_{PDVF}} + C_{E_{substrate}} + C_{E_{P\,oly\,\infty}} \quad (9)$$

The equilibrium circuit of our proposed multilayer interdigital capacitor model is shown in Figure 10.

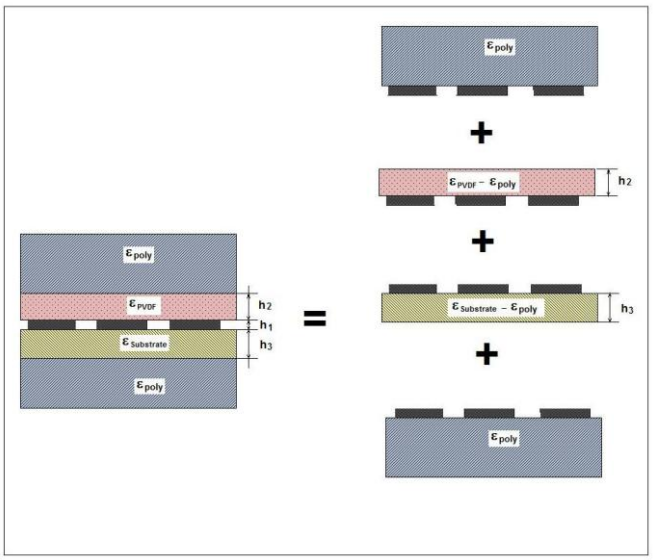

Fig. 10. The proposed three-layered IDC capacitor model

The capacitances of the IDC unit cell with infinite layer and finite layer at interior or exterior electrodes are described using a complete elliptic integral of the first kind shown in Table II; where K(k) is the complete elliptic integral of the first kind with modulus k, k' is the complementary modulus of k, v_2 and v_3 are the Elliptic theta functions, $sn(z,k)$ is the Jacobi elliptic function of modulus k, $\lambda = 2(g_c + w_c)$ is the spatial wavelengh, and the adimensional parameter which the capacitance of the IDC depends on is the metal ratio which can be calculated as $\eta = w_c/(g_c + w_c) = 2w_c/\lambda$, $r = h/\lambda$ where h is the thickness of the dielectric layer and ε_0 is the permittivity of free space. The above equations are written for the case of a thick substrate (the thickness of the substrate must be much higher than $\lambda/2$ if we want to consider it like a infinite layer).

Table 2. Detailed equations needed for the calculation of CI and CE for a finite layer as well as for an infinite layers

	Interior Electrodes	Exterior Electrodes
Finite Layer	$C_I=\varepsilon_0\varepsilon_r\frac{K(k_I)}{K(k_I')}$	$C_E=\varepsilon_0\varepsilon_r\frac{K(k_E)}{K(k_E')}$
	$K_I'=\sqrt{1-{k_I}^2}$	$K_E'=\sqrt{1-{k_E}^2}$
	$k_I=t_2\sqrt{\frac{{t_4}^2-1}{{t_4}^2-{t_2}^2}}$	$k_E=\frac{1}{t_3}\sqrt{\frac{{t_4}^2-{t_3}^2}{{t_4}^2-1}}$
	$t_2=sn(K(k)\eta,k)$	$t_3=\cos h\left(\frac{\pi(1-\eta)}{8r}\right)$
	$t_4=\frac{1}{k}$	$t_4=\cos h\left(\frac{\pi(\eta+1)}{8r}\right)$
	$k=\left(\frac{v_2(0,q)}{v_3(0,q)}\right)^2$	$\eta=\frac{g_c}{g_c+w_c}=\frac{2g_c}{\lambda}$
	$q=exp(-4\pi r)$	$r=\frac{h}{\lambda}$
Infinite Layer	$C_I=\varepsilon_0\varepsilon_r\frac{K(k_I\infty)}{K(k_I'\infty)}$	$C_E=\varepsilon_0\varepsilon_r\frac{K(k_E\infty)}{K(k_E'\infty)}$
	$K_I\infty=\sin\left(\frac{\pi}{2}\eta\right)$	$K_E\infty=\frac{2\sqrt{\eta}}{1+\eta}$

The general expressions used for the estimation of multilayer inter-digital electrode capacitance can be found in literature [10]. It is of the form,The total capacitance of a IDC-S is given by:

$$C_{IDC}=(N-3)\frac{C_{I,IDC}}{2}+2\frac{C_{I,IDC}C_{E,IDC}}{C_{I,IDC}+C_{E,IDC}} \tag{10}$$

Where $C_{I,IDC}$ and $C_{E,IDC}$ are developed using the equations and the partial capacitance technique [10]. A IDC-S with a thick substrate of relative permittivity ε_s, one sensitive layer of relative permittivity ε_{PVDF}, and the infinite protective layer of relative permittivity ε_{Poly} will have their total capacitances $C_{I,IDC}$ (Interior electrodes capacitance) and $C_{E,IDC}$ (Exterior electrodes capacitance), using the connotation shown in the figure 10 and equations 8 and 9 we have: given by:

$$C_{I,IDC}=\varepsilon_0 L[2\varepsilon_{poly}\frac{K(k_{poly\infty})}{K(k'_{poly\infty})}+(\varepsilon_{PVDF}-\varepsilon_{poly})\frac{K(k_{I,PVDF})}{K(k'_{I,PVDF})}+(\varepsilon_S-\varepsilon_{poly})\frac{K(k_{I,S})}{K(k'_{I,S})}] \tag{11}$$

$$C_{E,IDC}=\varepsilon_0 L[2\varepsilon_{poly}\frac{K(k_{poly\infty})}{K(k'_{poly\infty})})+(\varepsilon_{PVDF}-\varepsilon_{poly})\frac{K(k_{E,PVDF})}{K(k'_{E,PVDF})}+(\varepsilon_S-\varepsilon_{poly})\frac{K(k_{E,S})}{K(k'_{E,S})}] \tag{12}$$

The predicted capacitance is calculated based on equations derived from conformal mapping theory. In [10],results from this method have been compared to other methods, which show a great coherence with the test results. These equations were directly used in our model. The capacitance predicted by the equations is shown in Figure 11 with respect to η and the design parameter in table III.

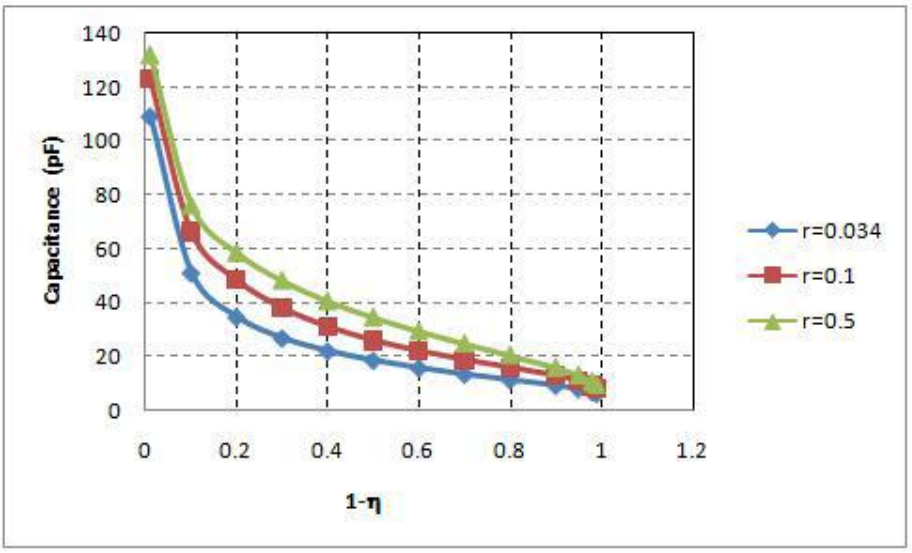

Fig. 11. Capacitance as a funtion of η and design parameter in the table III

Table 3.IDC Design Parameter

DESIGN PARAMETER	VALUE
εσ	3.9
εψλοπ	2.25
ε ΦΔ ςΠ	10
εo	8:854x10^-12 F/m
N	26
LC	24.1 mm
h1	35 μm
h2	110 μm
h3	100 μm
WC	800 μm
GC	800 μm

3.3.2 Inductance estimation

The proposed battery-free wireless pressure sensor has an circular inductive coil, the coil was formed by winding (7 turns) an coated copper wire AWG 23($\varphi 0.6\,mm$), forming a circular loop (40mm dia).

The self-inductance of circular loop of round wire has low frequency inductance that can be estimated by [11].

$$L_r \approx n^2 \mu_0 R\left[\ln\left(\frac{8R}{a}\right) - 1.75\right] \tag{11}$$

Where n means the inductor turns, R indicates the loop radius, a corresponds to the wire

radius, and the magnetic permeability of free space $\mu_0 = 4\pi x10^{-7} H/m$ .the inductance of the proposed pressure sensor is $5.57\ \mu H$.

3.3 Sensor fabrication and experimental results

3.3.1 Calibration Results of Parallel Plate Pressure Sensors

For the parallel plate pressure sensor proposed were done two experiments for each material (Polyurethane and PDMS). In the Figures 2-4 and 2-5 are shown the experimental relationship between the pressure applied and the resonant frequency of the sensor.

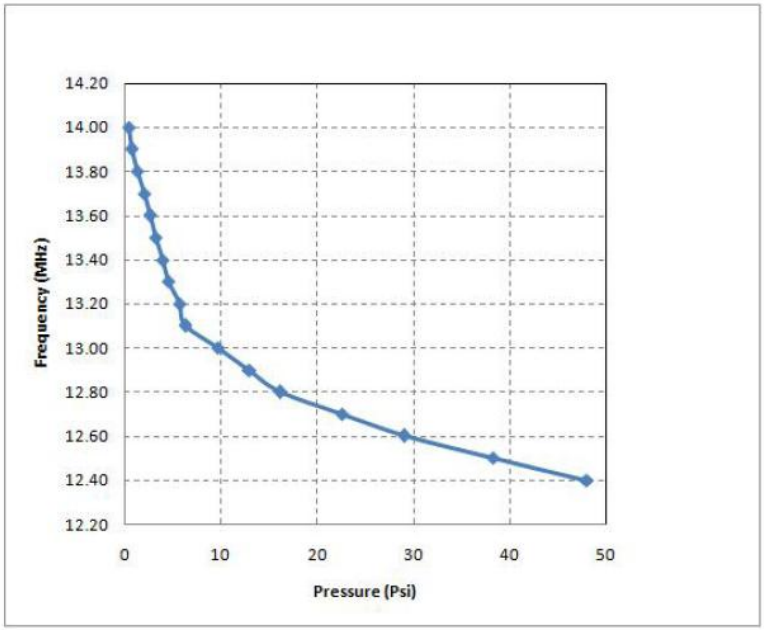

Figure 2-4: Resonant frequency of the sensor vs. pressure measured with the wireless set-up for POLYURETHANE material

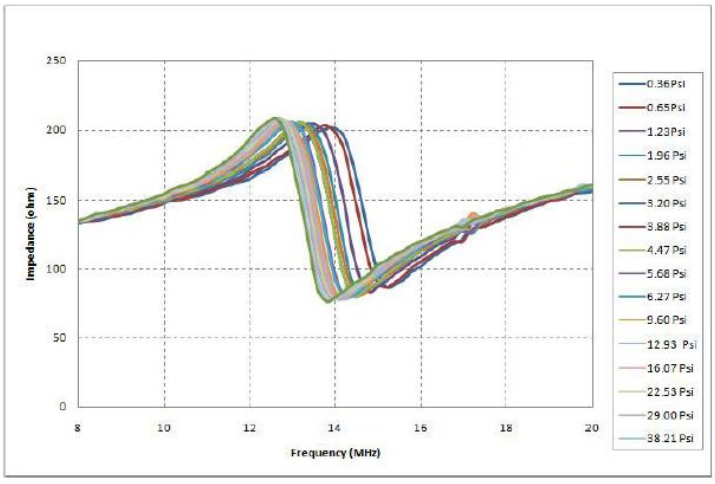

Figure 2-5: Resonant frequency of the sensor vs. pressure measured with the wireless set-up for PDMS material

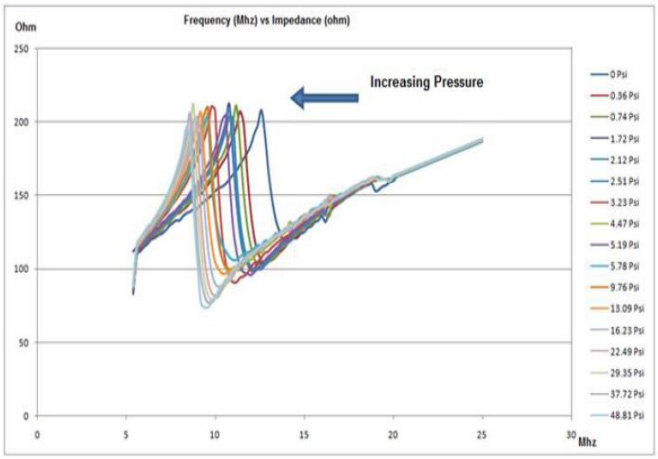

Figure 2-6: Resonant frequency of the sensor vs. impedance response of the reader measured with the wireless set-up for PDMS material

The interdigital pressure sensing element is fabricated using photolithography processes on a DuPont Pyralux AC single-side copper-clad laminate which is an all-polyimide composite of a polyimide thick film on a copper foil with substrate and rolled-annealed (RA) copper foil thickness of $25\,\mu m$ and $1\,18\,\mu m$ respectively. The fabricated sensor prototype is shown in the Figure 12.

The experimental test for the developed sensor was carried out in a compression test machine. This machine consists of a worm gear loading system , to generates a compressive force on the pressure sensor . This compression force is measured by a load cell and converted into voltage signal, and then send out to an external data acquisition device. Experimental setup is shown in the Figure 13, a potable reader antenna was set near to the inductor coil of the test sensor, read sensor's resonant frequency wirelessly and powerlessly.

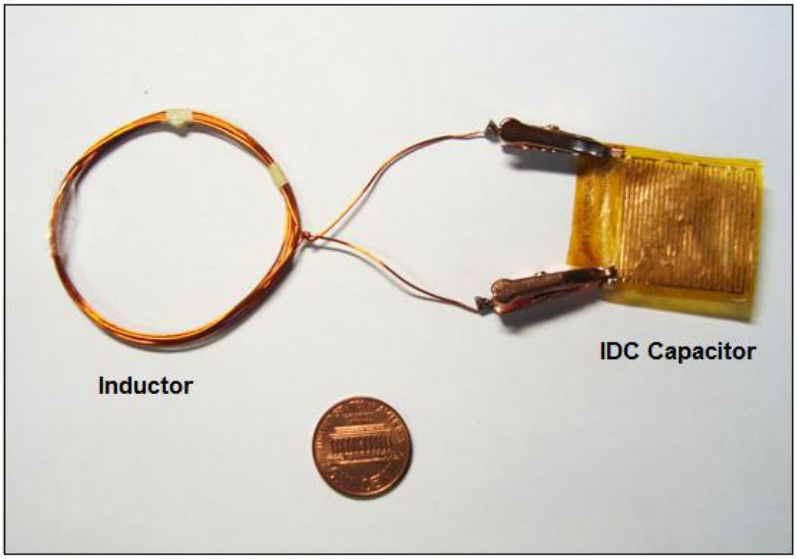

Fig.12: Sensor Prototype of IDC pressure sensor

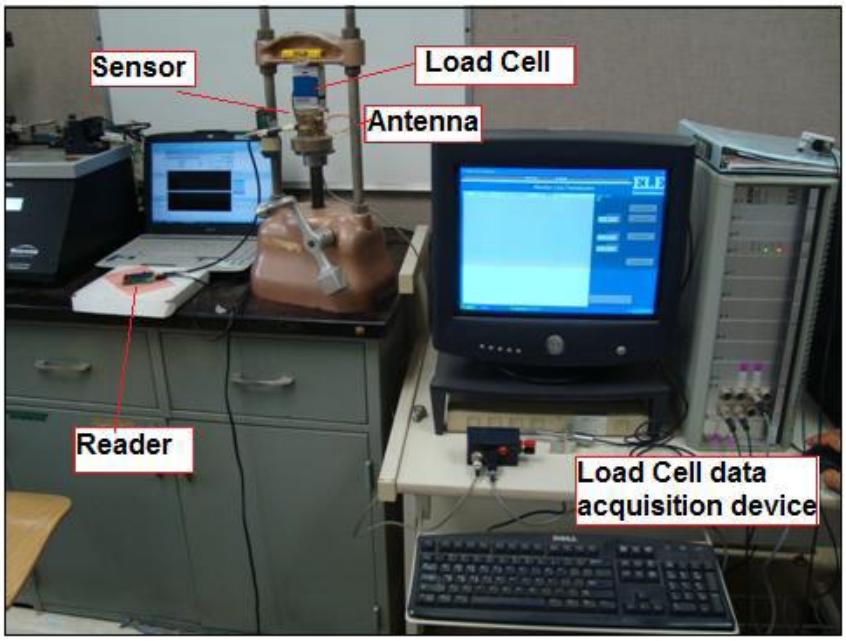

Fig.13. Experimental setup up

Figure 13 shows the experimental relationship between the pressure applied and the resonant frequency of the fabricated sensor.

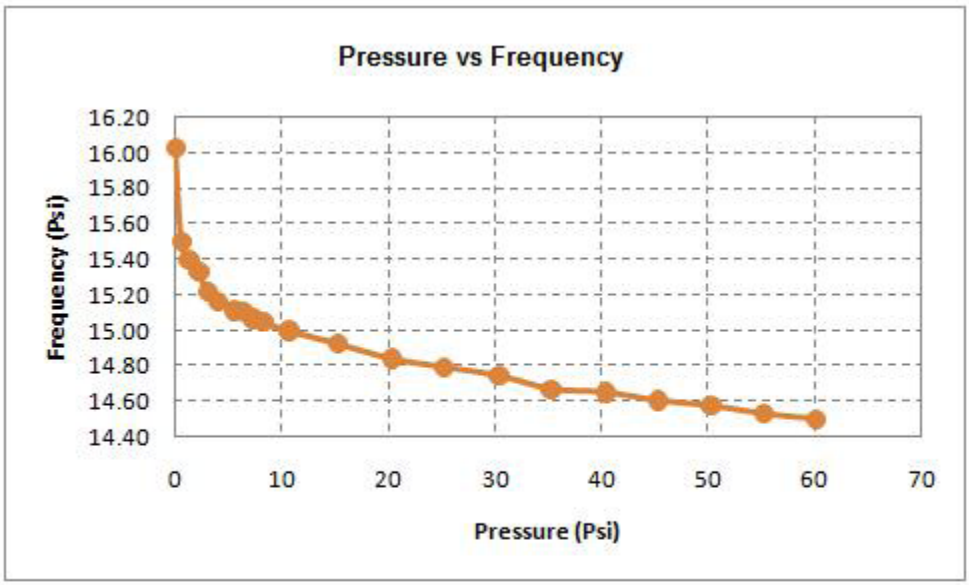

Fig.14. Sensor's resonant frequency vs. pressure measured

3.4 Conclusion

This report presents the development of a novel battery-free wireless pressure sensor. Based on the physical model of a spiral inductor and an interdigital capacitor, the pressure sensing mechanism, design and fabrication of the IDC based battery-free pressure sensor has been studied. The result of this research project has demostrated feacibility of the proposed

pressure sensor and good sensitivity. Battery-free and wireless pressure sensing can be realized without requiring physical connection, power supplies and active elements in the sensor circuit.

4. RFID based passive wireless humidity sensor

This report summarizes the development of a prototype RFID humidity sensor capable of passive wireless sensing through far-field backscatter coupling. A commercial available UHF RFID tag is employed as a sensing platform to receive the power and to reflect the sensed data back to the RFID reader. A humidity sensitive polyimide film is incorporated onto the top surface of the RFID tag for humidity sensing. The prototype sensor demonstrated that power required to activate the sensor tag is a linear function of humidity level and the maximum sensing distance between the reader antenna and the RFID humidity sensor tag reaches to about 1.5 m. Due to its unique features of low cost, battery-less wireless operation, maintenances-free, and disposable, the RFID humidity sensor can be integrated into industrial environment for humidity monitoring.

4.1 Principles of Operation

Radio frequency identification (RFID) sensing has attracted considerable attention in recent years due to its low cost and passive wireless features. RFID tags can be classified into two categories: *active* and *passive*. Active tags require a power source, a powered infrastructure or use energy stored in an integrated battery. Passive RFID tags do not contain a discrete power source, but derive their energy from an incident RF signal and reflect the RF carrier back to the reader. Tag information is wirelessly transferred as the reflected signal is modulated by the RFID tag. RFID sensing is expected to be an important platform in the realisation of passive wireless ubiquitous sensing. Integrating various sensing materials into low cost RFID based passive wireless platform will be an innovative approach to develop passive wireless sensor technologies.

Two fundamentally different RFID based passive wireless sensing platforms exist for built environmental monitoring: near-field inductive coupling technology and far-field backscatter coupling technology. Both transfer enough power from reader to a remote tag, sustain its operation and receive data through various modulation techniques.

Faraday's principle of magnetic induction is the basis of near-field coupling between a RFID reader and tag. It is the most straightforward approach for implementing a passive RFID sensing system. This platform is typically realized by employing an inductive coil (L) and a sensitive capacitor (C) formed LC resonant tank circuit incorporated with sensitive materials. The sensed information is transmitted back to the reader using load modulation. The drawback of this technology is its limited sensing distance in the order of 10 mm.

RFID sensing platform based on far-field coupling technology is back scattering. Electromagnetic wave propagates from a dipole antenna attached to the reader to a RFID tag, as shown in figure 1. A smaller dipole antenna in the tag receives this energy, rectify this potential and link it to a capacitor, which will result in an accumulation of energy in order to power the tag electronics. If the antenna of the tag is designed with precise dimensions, it can be tuned to a particular frequency and absorb most of the energy that reaches it at that frequency. However, if an impedance mismatch occurs at this frequency, the antenna will

reflect back some of the energy toward the reader, which can then detect the energy using a sensitive radio receiver. By changing the antenna's impedance over time, the tag can reflect back some incoming signal in a pattern that encodes the tag's stored data.

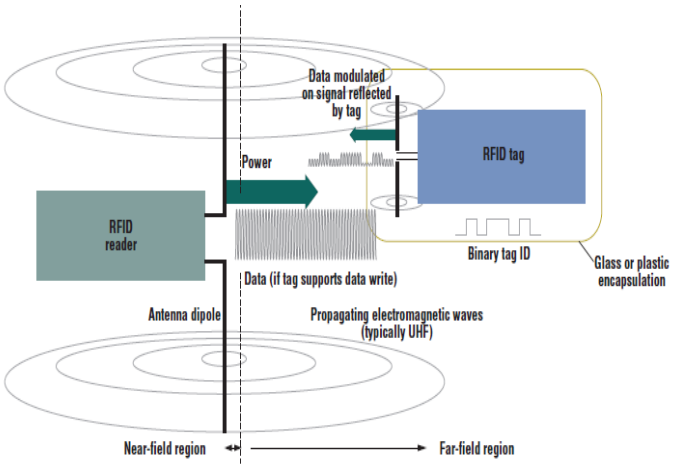

Figure 1. Far-field backscatter coupling principle

4.2 RFID Humidity Sensing Tag

A UHF RFID tag developed by KSW Microtec in Germany is adapted for this study. As we know that the performance of this low cost RFID tags, constructed with simple one-layer antennas, is very sensitive to the surrounding environment and especially to nearby metallic surfaces and water. Water content nearby the RFID antenna will directly cause ohmic losses in the antennas and also change its resonance frequency. Depositing a humidity sensitive material on the RFID antenna will absorb water and change the water vapour concentration in the RFID antenna. This results in a performance change of the RFID tag. Monitoring the change could detect humidity level in the built environment where the RFID tag is embedded.

The materials used for humidity sensing can be grouped into three types: electrolytes, organic polymers and ceramics. Polymer films, because of their durability, flexibility and ease of fabrication, have been used in a variety of humidity sensors. Polymers can be used in either a capacitive or resistive mode. Of the conducting polymers used in humidity sensors, the most commonly used is polyimide, but a variety of other conducting polymers have also been used. Humidity sensors can also use the change in the capacitance of a polymer as a function of humidity due to changes in the dielectric properties or expansion, both of which can be measured using a parallel-plate capacitor. However, the expansion of a polymer, such as polyimide, can also be measured by placing a piezoresistive element adjacent to the expanding polymer. Another approach is to measure the amount of water absorbed in the polymer film using a SAW oscillator. The most common commercially available sensors are polymer-based capacitive sensors. In this study, PI-2723 polyimide, provided by DuPont, is used to paint on the surface of the RFID antenna. Figure 2 shows an original KSW RFID tag and the tag with polyimide humidity sensing material.

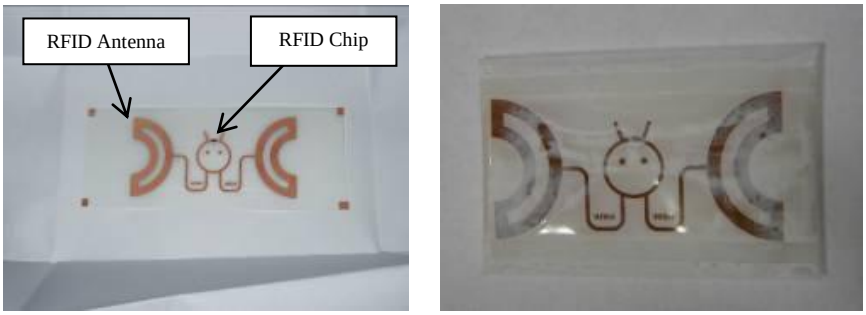

(a) Commercial available RFID tag (b) The tag with humidity sensing material

Figure 2. Wireless RFID Humidity Sensing Tag

4.3 Experimental Details

Figure 3 shows a schematic of the experimental setup. The sensor characterization system is a commercial passive RFID system classified as Generation 2 and operating in the license free EU band at 865-868 MHz. the system consists of a signal generator, a spectrum analyzer, a RFID reader antenna, and the RFID humidity sensor tag. The reader antenna was connected to the signal generator and spectrum analyzer from HP Agilent by a circulator. Detailed list of the equipment and operation condition are given in the table 1.

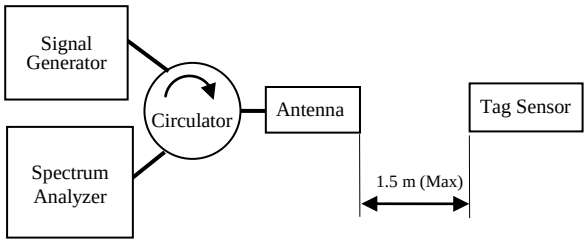

Figure 3. Schematic of the experimental setup

The UHF RFID tag with polyimide humidity sensitive coating was characterized as a passive wireless humidity sensor in an ordinary RF lab where temperature is well controlled. The humidity absorbing paper was placed on the tag and several drops of water was added to the humidity absorbing paper and distributed over the sensor tag at the beginning of each characterization. The reader antenna was positioned at fixed distance of 1.5 m away in front of the RFID tag and the sensor tag was in upright position so that the reader antenna had exactly the same distance to the RFID tag. The performance of the tag was monitored at different level of humidity by adding water or drying the humidity absorbing paper.

Table 1. List of equipment and operating condition

Signal Generator	Agilent E4438C, Signal Generator
Spectrum Analyzer	Agilent E4448A, Spectrum Analyzer
Antenna	Kathrein UHF-RFID Antenne, (5201001) 865-870 MHz, 8.5 dBic
Sensor Tag	KSW UHF RFID tag with humidity sensing coating
Operating	868 MHz

frequency	

Figure 4 shows a front view of the sensor tag under the test.

Figure 4. RFID humidity sensor tag under Test

A photo of the experimental system is illustrated in the figure 5.

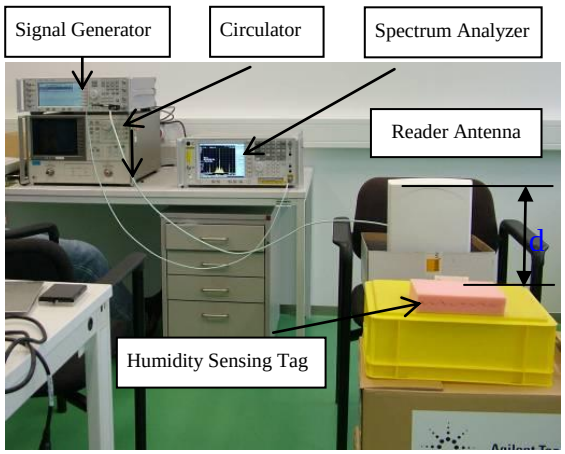

Figure 5. Passive wireless sensing experimental setup

In a humid environment the water vapor concentration is high in the polyimide sensing material, which causes degradation to the sensor tag's antenna in terms of dielectric losses and change of input impedance. This results in a different power requirement to activate the sensor tag. The experimental system allows control of the antenna output power and a threshold level for what output power is necessary to remotely power up the passive wireless humidity sensor tag.

4.4 Results and discussions

In the first characterization the sensor tag was characterized when the water absorbing paper was directly supplied with several drops of water at beginning, and the sensor tag was activated in every five minutes. In order to record the power level that is required to activate the tag at the signal generator, the output power of the signal generator was increased in 0.10 dBm step by step until the response signal of the tag gets visible on the spectrum analyzer, which indicates that the sensor is activated. Figure 6 shows the 868 MHz signal and the response of the tag. The large peak in the centre is the 868 MHz signal from the signal generator and the two smaller peaks are the reflected response from the sensor tag. As the

moisture absorbing paper becomes dryer after five minutes, same experiment was repeated. The result of the first experiment is shown in Figure 7.

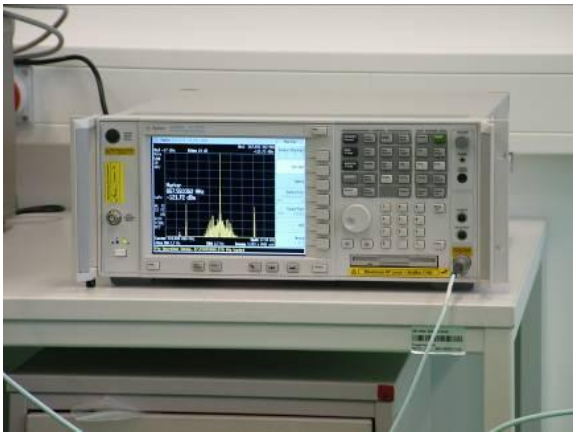

Figure 6. Screen of the spectrum analyzer

At the beginning of the characterization, water vapor concentration was high, changes in both the real and imaginary parts of the sensing material dielectric constant caused degradation of sensor's antenna performance, and the tag antenna operated with low efficiency and its backscattered signal strength of the RFID system is proportional to the relative humidity in the humidity sensing material. Power required in first tag activation is about 7.6 dBm and 15 minute later as the water absorbing paper get dryer, the power required to activate the sensor tag is about 3 dBm. The Required activation power and relative humidity relationship is clearly seen in figure 7.

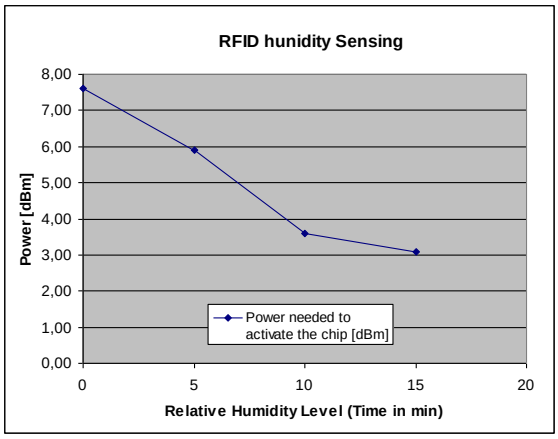

Figure 7. Power as a function of relative humidity

In the second characterization a new dry water absorbing paper was placed on the tag. Then one drop of water was added to the paper at the time and the necessary power to activate the tag was determined. Thereafter, one additional drop of water was added to the paper and again the power that activated the tag was determined. The number of water drops was increased until the maximum power of the signal generator was reached. At the time of malfunction the maximum transmitted power was about 19 dBm. **Error! Reference source not found.** Figure 8 shows the result of the second characterisation.

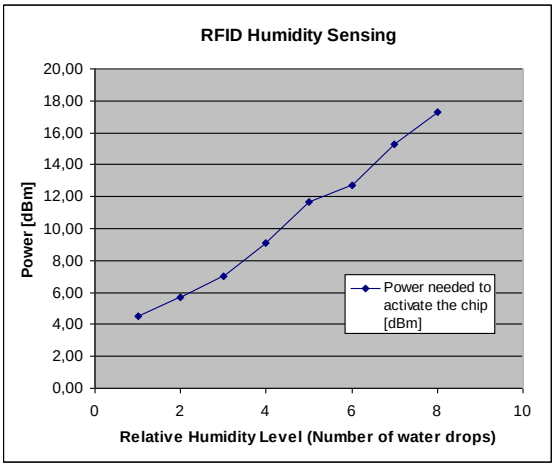

Figure 8. Power as a function of relative humidity

As it is shown in figure 8, the power necessary to activate the sensor tag is nearly linear function of the number of water drops. Unfortunately these characterisations were not carried out in a climate chamber where the relative humidity is well controlled and precisely indicated. However, as a proof-of-concept experiment, the results show a promising that the prototype RFID humidity sensor is a promising technology for passive wireless humidity sensing in the built environment.

A prototype RFID humidity sensor has been developed and the sensor characterizations have demonstrated that a commercial available UHF RFID tag incorporated with polyimide film can be employed as a sensing platform for developing a passive wireless humidity sensor. Due to its unique features of low cost, battery-less wireless operation, maintenances-free, and disposable, the RFID humidity sensor can be integrated into industrial environment for humidity monitoring.

5. Zigbee enable wireless temperature sensor network

This is a preliminary report of development of a wireless sensor network for advanced fossil-fuel based power generation application during this research period. The prototype wireless sensor network consisting of a set of sensor nodes for digital and analog data sensing, a route node for sending and receiving message, and a base station for data storing and analyzing was designed, implemented and tested. The sensor network is developed based on Xbee ^{TM} 2.5 RF modules, which were engineered to operate within IEEE 802.15.4/Zigbee protocol and support the unique needs of low-cost, low-power wireless sensor networks, and Arduino open source hardware and software provides sensor interface programming and easy implementation. A 24-hour run evaluation of this network was carried out in a machine room and results are demonstrated in this report.

5.1 Introduction

Wireless sensor network technology can provide optimal and integrated solution for distributed data collecting, delivering and analyzing in many applications including advanced fossil-fuel based power generation application.

The developing prototype of the wireless sensor network consists of a set of sensor nodes, a route node and a based station. Compared with many short-range wireless communication protocols such as Bluetooth, WiFi, Zigbee standard is more suitable for advanced fossil-fuel based power generation application. The wireless sensor network is developed based on Xbee^{TM} 2.5 RF modules, which were engineered to operate within IEEE 802.15.4/Zigbee protocol and support the unique needs of low-cost, low-power wireless sensor networks. In ZigBee network, there are three type nodes: coordinator, route and end device. All Zigbee network must have one and only one coordinator, which can select the frequency channel, start network, and allow other nodes to join it and other service. An end device and router are used to send and receive messages. Differently, a router can relay messages and allow the child node t connect to it. In our application, the network structure is designed cluster tree topology, which consists of a coordinator and a set of routers and end devices, as illustrated in Figure 1. Base station node is configured as the coordinator. A few sensor nodes are defined as the routers, while other sensor nodes are defined as end devices. In the network design the sensor nodes acting as end devices are powered by batteries in order to reduce the cost. The Arduino open source hardware and software provides sensor interface and programming support to aid easy application development.

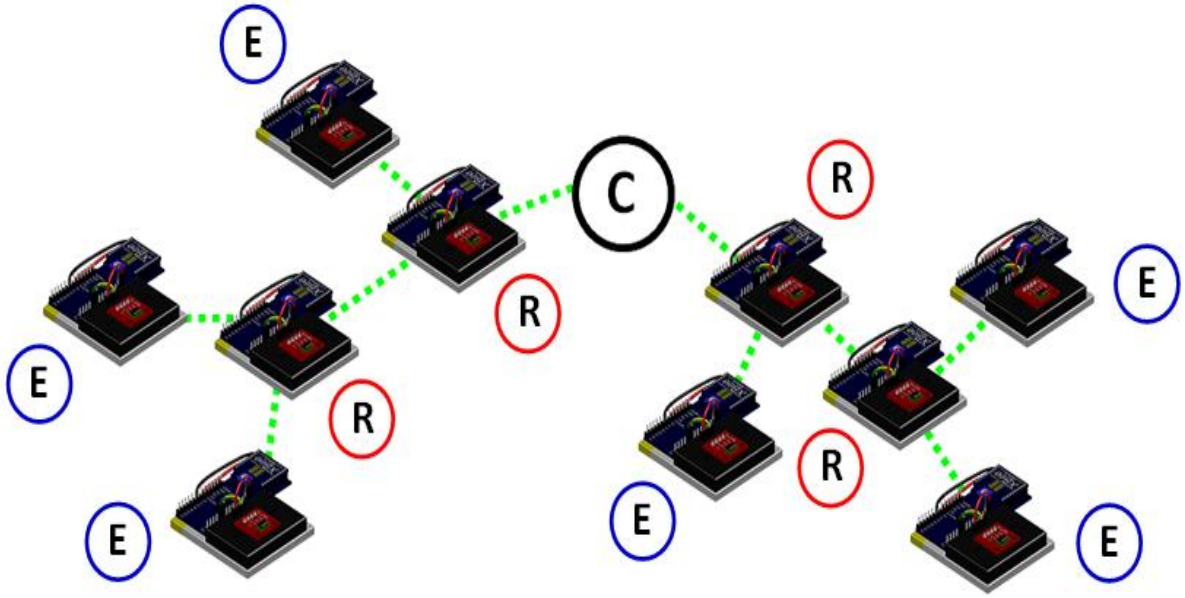

Figure 1 . ZigBee wireless sensor network topology

Where: Coordinator (C), Routers (R) and End Devices (E)**.**

5.2 Network Hardware Design

5.2.1 Sensing Unit

The wireless sensor network to be developed will be used for advanced fossil-fuel based power generation application. To demonstrate the frame work of the sensor network, the sensor employed for this task was the Sensirion SHT15 temperature and humidity sensor, see Figure 2. This sensor employs a 2-Wire interface and has a response time of less than 4 seconds and around 40 μW of power consumption.

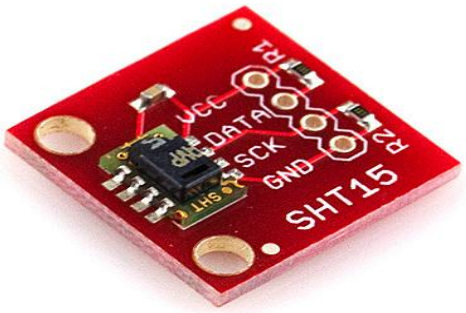

Figure 2. IC temperature and humidity sensor

5.2.2 Sensor Interface Unit

The Arduino Fio shown in Figure 3 is used for sensor interface. It is based on AVR's ATMega 328P microcontroller. The board houses 8 analog pins and 14 digital pins for input and output operations, supporting SPI and I2C communication on certain pins. This microcontroller includes an on-board charging circuit for Lithium Polymer battery, which is an advantage if Lithium Battery technology is used. The role of the microcontroller in the wireless sensor networks will be to poll the on board sensors for data, arrange it using the developed packet protocol and send it off to the RF module to be transmitted to the data sink. Furthermore, the data can be time stamped on board if necessary.

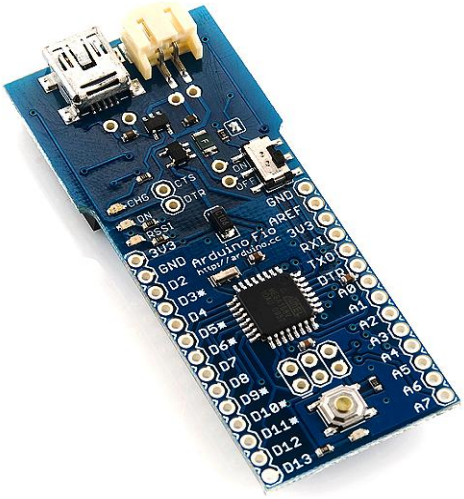

Figure 3. Sensor interface unit

5.2.3 Wireless Communication Unit

The communication unit used for the prototype was an Xbee ZB 2mW ZigBee Pro RF Module. This module was designed for applications where low power consumption was paramount. It also supports use of the ZigBee Standard, which provides a robust mesh networking architecture needed for the multi-hop cluster hierarchy presented. This wireless module integrates seamlessly with the Arduino Fio board. The RF module operates in the 2.4 GHz band with 16 direct sequence channels. Also, since the ZigBee standard is stacked on top of the IEEE 802.11.4 standard, it supports 16-bit and 64-bit addressing for each node. In total, each channel has 65,000 unique network addresses while supporting up to 250 bps data rate. XBee modules consume 38-40mA when transmitting, and 35-40mA when in receiving mode. This makes the radio module the most critical component of the wireless node from a power consumption viewpoint.

Figure 4. wireless communication unit

5.2.4 Power Unit

The prototype sensor node was designed to work with a 2000 mAh, 3.7 V Lithium Polymer battery. This kind of battery was employed due to its long life when taking into account the application and the fact that the Arduino Fio includes a Lithium Polymer battery port. Also, Lithium Polymer batteries are rechargeable, which is of interest for continued deployment application.

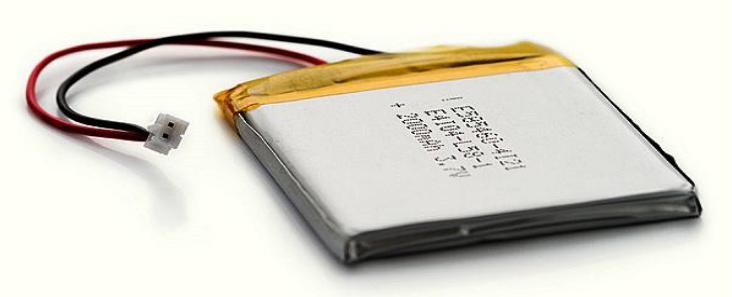

Figure 5. Lithium Polymer battery

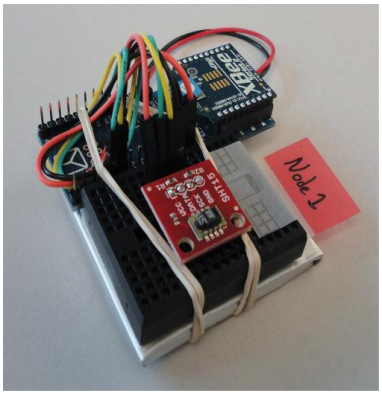

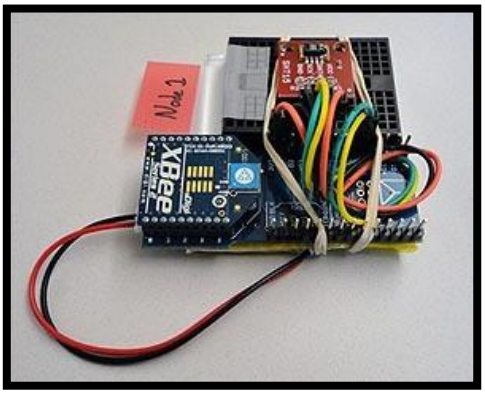

Figure 5. Prototype wireless sensor node with all hardware components integrated.

5.3 Evaluation Results

The performance of the wireless sensor network prototype was placed in a machine room, 24 hour run data was collected. Figures 6 and 7 show partial results of tempeature and humidity readings during 24 hours evaluation from sensor node 2 and node 5.

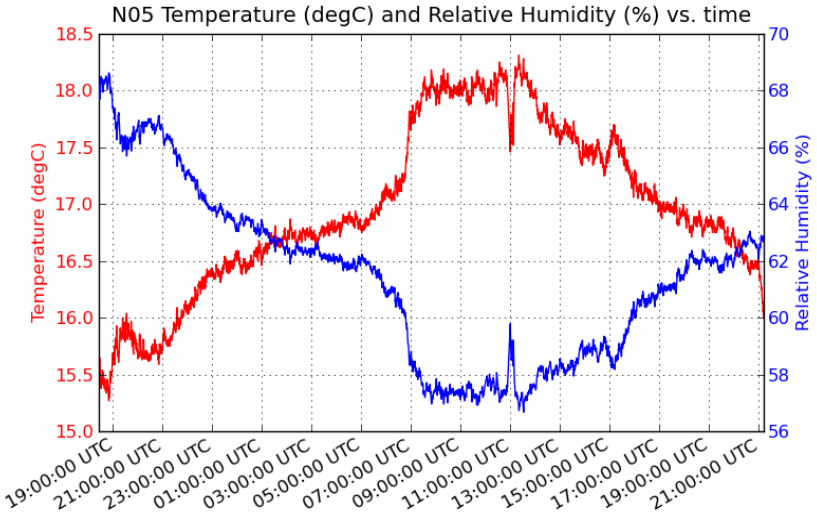

Figure 6: Temperature and humidity reading of sensor node 5

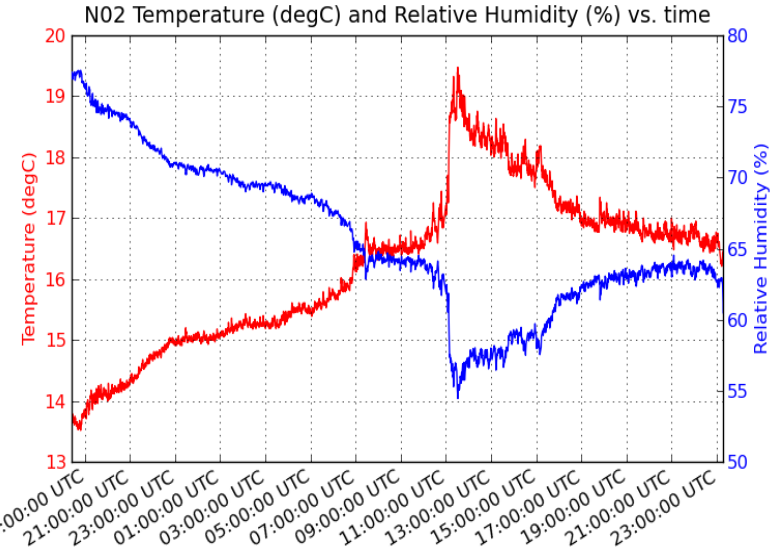

Figure 6: Temperature and humidity reading of sensor node 6

5.4 Conclusions

A prototype wireless sensor network has been developed, and provide optimal and integrated solution for distributed analog and digital sensor data collecting, delivering and analyzing for advanced fossil-fuel based power generation application.

1. Executive summary

In this research period, we continue to develop wireless sensor network for advanced fossil-fuel based power generation applications. The wireless sensor network developed has two different wireless network architectures. Multi-Hop Multi-Point to Point Network design is to monitor large area environmental profile and Multi-Hop Cluster Network architecture is

used to capture critical information at concentrated area of any application. Each network is composed of a suite of sensor nodes to sense critical parameter such temperature, strain, pressure etc, route node for relay the sensed data and a coordinator node to start the network, receive the data and process the data. Software has been developed based on managing sensor interface, ZigBee wireless communication and data management.

2. Results of working during reporting period

A. Network Architecture Design

A wireless sensor network consists of sensor nodes, interface circuit, power supply, and RF radio module. Compared with many short-range wireless communication protocols such as Bluetooth and WiFi, Zigbee standard is more suitable for advanced fossil-fuel based power generation applications. The wireless sensor network in this study is designed having two different wireless network architectures, as show in Figure 1. Multi-Hop Multi-Point to Point Network design is to monitor large area environmental profile and Multi-Hop Cluster Network architecture is used to capture temperature and humidity information at concentrated area of the rack. Each network is composed of a suite of sensor nodes to sense environmental information, route node for relay the sensed data and a coordinator node to start the network, receive the data and process the data. Software has been developed based on managing Arduino sensor interface, ZigBee wireless communication and data management.

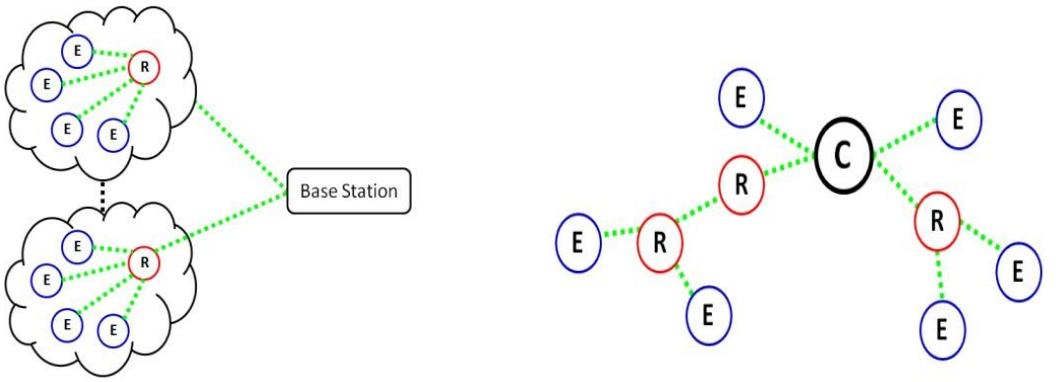

Multi-Hop Cluster Network

Multi-Hop Multi-Point to Point Network

Figure 1. Architecture diagram of the proposed wireless network

B. Network Hardware Design

As the core of the wireless sensor network (WSN) hardware, the WSN node is usually composed of a series of basic sensing element, sensor interface circuit, power supply and radio communication module.

Sensing Unit

The prototype wireless sensor network is used for monitoring of environmental data relevant to the advanced fossil-fuel based power generation applications. For this purpose, Sensirion SHT15 temperature and humidity sensors are selected. This sensor employs a 2-Wire interface and has a response time of less than 4 seconds and around 40 μW of power consumption.

Sensor Interface Unit

The Arduino Fio open source hardware is adopted as sensor interface. This platform is based on AVR's ATMega 328P microcontroller, and the board houses 8 analog pins and 14 digital pins for input and output operations, supporting SPI and I2C communication on certain pins. The role of the microcontroller in the wireless sensor network is to poll the on board sensors data, arrange it using the developed packet protocol and send it off to the RF module to be transmitted to the route nodes. Furthermore, the data can be time stamped on board if necessary.

Wireless Communication Unit

Wireless sensor network is developed based on Xbee ™ 2.5 RF modules, which were engineered to operate within IEEE 802.15.4/Zigbee protocol and support the unique needs of low-cost, low-power wireless sensor networks. ZigBee defines three different device types. Coordinator is responsible for establishing the operating channel and PAN ID for an entire network. Once established, the coordinator can form a network by allowing routers and end devices to join to it. Router maintains network information and uses this information to determine the best route for a data packet, end device always interacts with their parent nodes to receive or transmit data. Differently, a router can relay messages and allow the child node to connect to it. End nodes are intended to sleep periodically and therefore have no routing capacity.

Xbee ™ 2.5 RF modules supports use of the ZigBee Standard, which provides a robust mesh networking architecture needed for the multi-hop multi-point to-point network and multi-hop cluster hierarchy presented. This wireless module integrates seamlessly with the Arduino Fio board used as well. The RF module operates in the 2.4 GHz band with 16 direct sequence channels. Also, since the ZigBee standard is stacked on top of the IEEE 802.11.4 standard, it supports 16-bit and 64-bit addressing for each node. In total, each channel has 65,000 unique network addresses while supporting up to 250 bps data rate. XBee modules consume 38-40mA when transmitting and 35-40mA when in receiving mode. This makes the radio module the most critical component of the wireless node from a power consumption viewpoint.

Power Supply

The prototype sensor node is powered by a 2000 mAh, 3.7 V Lithium Polymer battery. This battery is selected due to its long battery life when taking into account the application and the fact that the Arduino Fio includes a Lithium Polymer battery port.

C. Network Software Design

There are three software developed in this wireless sensor network in order to establish the sensor interface, configure mesh network and manage the sensed data for data receiving, storing and displaying.

Sensor Interface Software Design

The design of Arduino Fio open-source software is to read temperature and humidity strings from the sensors, convert these strings into numerical values with specific data format, manage sensor ID, and develop data pocket to be send it off to the RF module, and then, Arduino Fio is programmed by Arduino Integrated Development Environment with FTDI USB Cable. The Arduino open source software provides sensor interface programming to aid easy application development.

Zigbee RF Module Configuration

To realize the designed network architectures, Xbee modules were configured to behave coordinator, routers as well as end devices depending of the circumstances. The XBee Series 2 is designed to add mesh networking to the underlying 802.15.4 radio. The mesh network consists of a coordinator node which receives data from its surrounding router/end nodes. The coordinator has the unique function of forming a network and is responsible for establishing the operating channel and PAN ID. Once established, the coordinator can form a network by allowing end devices to join to it. Since all XBee modules come with a default PAN ID, therefore, an unique PAN ID was assigned to each XBee module in order to avoid to have communication problem with other sensor networks in the same area. After choosing the correct function set at X-CTU, XBee configuration software, provided by the Digi website and the new configuration will be downloaded into the RF modules.

Data Management System Software Design

Three data management programs were developed using MATLAB programming language. The first program is to read real-time data strings from coordinator nodes, convert them to numerical values, detect type of information (temperature or humidity), put time stamps on each received sensor data, and saved the data into the database file. Second program is developed to organize the database into separate temperature data file and humidity data file. The third program is to visualize the sensed data. This is an easy-to-use graphic interface with drop-down menu to select sensor nodes, temperature or humidity file, and the program has a button to refresh the screen in order to show all the data in the same screen.

D. Conclusions

Figure 2 shows 10 prototype networked wireless nodes with temperature and humidity sensors. We can connect any type of sensors into this wireless sensor network.

Key Features of the developed wireless sensor network are

- High Performance
  - Up to 100 m/indoor and 1.6 km/outdoor.
  - RF data rate: 250,000 bps.
- Low Power
  - Tx current: 295 mA @3.3 v
  - Rx current: 45 mA @3.3 v
  - Power down current (Idle mode): < 1 μA @25 ℃
  - Advanced Networking Capability
  - 16 channels
  - 65,000 unique network address
  - Self-routing, self-healing and fault-tolerant mesh network.
  - 16 bit unique physical address for each sensor node.

- Sleep Mode
  - Both pin sleep and cyclic sleep allow the RF module to enter states of low power consumption when not in use.

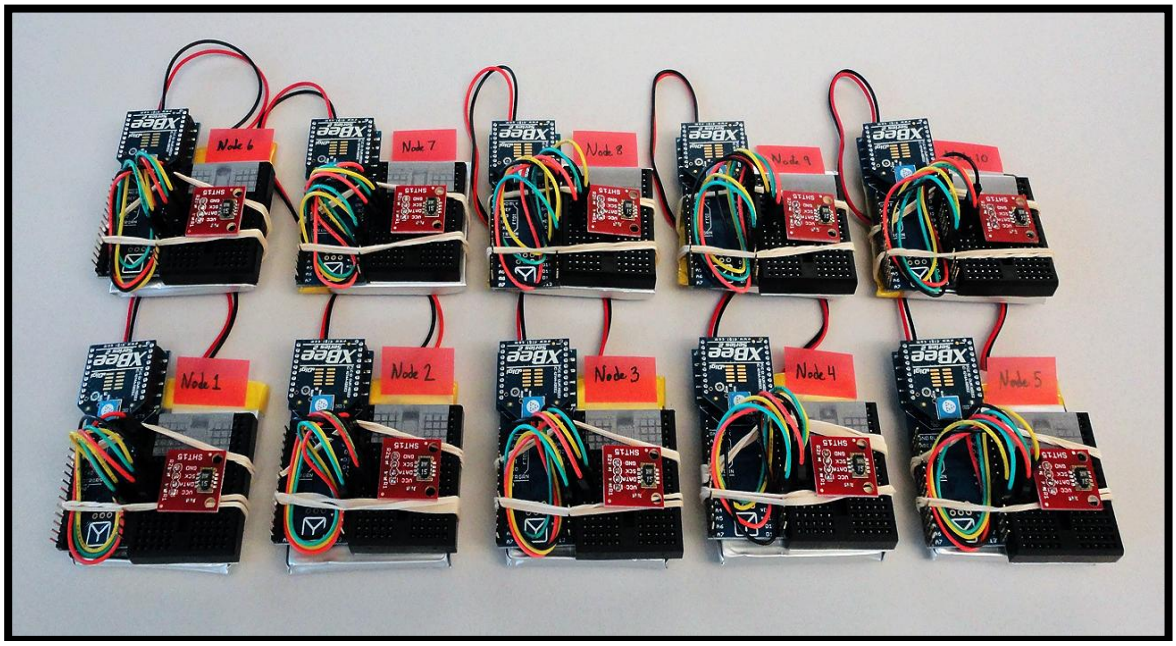

Figure 2. Networked Wireless Nodes with Temperature and Humidity Sensors

6. Preliminary study of passive wireless crack sensor

A novel passive wireless sensor, consisting of an interdigital sensing capacitor and a loop antenna as inductor antenna is proposed for crack monitoring. The abovementioned two components work together as an LC resonator whose resonant frequency is designed to change correspondingly with the size, shape, orientation, propagation and stages of the monitored crack. This corresponding frequency variation will be detected by a LC frequency reader by monitoring the impedance across the terminals of the wide bandwidth reader antenna. Thereafter this crack information will be retrieved and interpreted based on the received signal from the reader by the resonant frequency shift.

6.1 Introduction

In the recent years there has been an increasing interest in the use of sensing technologies for Structural health monitoring (SHM). SHM is the process of detecting and monitoring structural damages [1-4]. All structures undergo a process of damage and deterioration over a period of time. Extreme changes occur in operational environment, deterioration will be accelerated and ultimately lead to collapse of the whole structure. The resulted loss of human life and property can be devastating. Thus, it is of utmost importance to monitor the structural health of civil, aerospace structures to improve their reliability. SHM is especially important for those structures that are operating beyond their designed service life. SHM involves observation of the structure using one or more distributed sensors monitoring one or more properties of the structure. Some of the important properties that are used to quantify the health of a structure are fatigue cracks, strain, temperature and displacement. Among them, fatigue crack is considered as the major defects that emerge due to aging of structures.

However, these technologies require either physical connection of signal communication, battery power supply or expensive equipments for acquiring pressure information. These limitations make existing crack sensing technologies unsuitable for most of the structures health monitoring applications

In this project, crack monitoring will be accomplished by teaming up interdigital crack sensor and the remote reader. The crack signal is conveyed by the forms of the resonant frequency acquired by a remote antenna. Here, the remote antenna has dual function. While it performs the wireless communication, it also serves as a remote power supply for the sensor.

6.2 Crack sensor model

The design of the sensor relies on the properties especially resonant frequency f_0, which is a function of L_S, C_S and R_S, and the total capacitance C_S is a function of two dimensional parameters, η (metallization ratio) and r (layer thickness to wavelength ratio), L_C (length of electrodes) and N_C (number of electrodes), height of sensing layer and as well as the dielectric permittivity of each layer $C = C(\eta; r; \varepsilon_S; \varepsilon_{Steel}; h; t; L_C; N_C)$.

6.2.1 Capacitance estimation

Conformal mapping is one of the most frequently used approaches to transform an appropriate space region of IDC to a parallel plate capacitor geometry whose capacitance value can be calculated. Igreja [6] developed an analysis and analytical solution for IDC capacitance using conformal mapping.

Figure 1 shows a layout of the electrode plane and a schematic diagram of the cross-section of an interdigital capacitor sensor (IDC-S) with two interpenetrating comb electrodes. The gaps between electrodes have a width of g_C while the fingers have a width of w_C. Each comb electrode is connected to a fixed potential (either +V or −V) and has a number of fingers of length L_C. Where t is the thickness of the IDES, h is the thickness and "S" is the permittivity of the substrate. Here $\lambda = 2(g_c + w_c)$ is called IDC-S spatial wavelength. Metal ratio is another dimensional parameter vital to capacitance and can be calculated as $\eta = 2w_c/\lambda$.

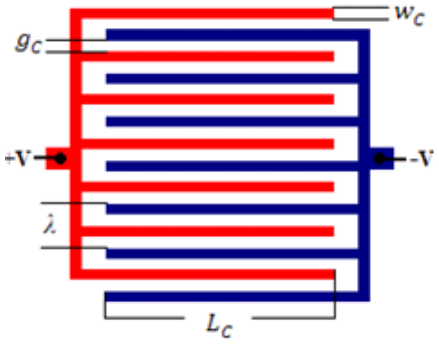

1.

Figure 1. (a)

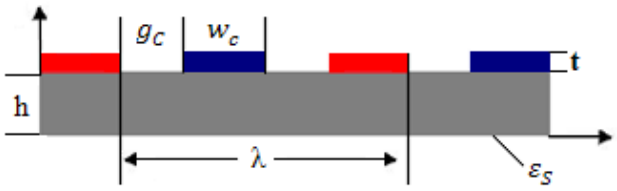

2.

Figure 1. (b)

Figure.1 (a) Layout of electrode plane and (b) IDC geometric dimensions

The proposed passive wireless IDC crack sensor will be bonded on the surface of test coupon. By symmetry, the perpendicular planes halfway between the electrodes are equipotential planes with *V=0*, it acts like an electric ground where electric field lines crossing normal to these planes shown in Figure 2.

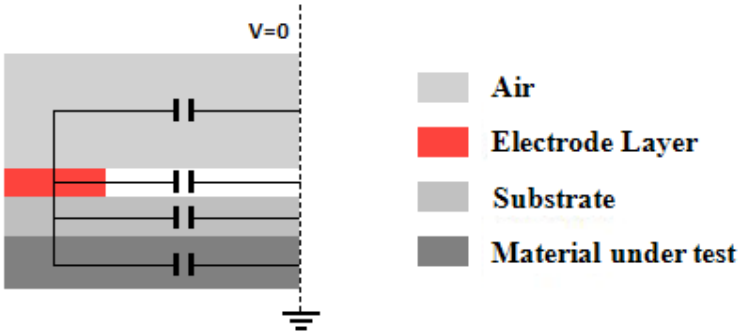

Figure.2 Half unit cell model of the proposed multilayer interdigital capacitor

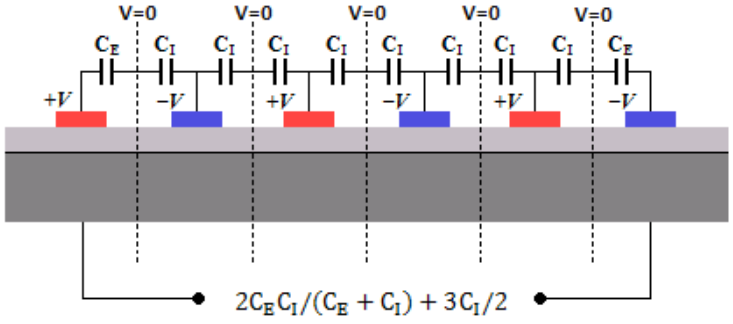

Figure.3 The equivalent circuit of the static capacitance of a multilayer interdigital capacitor

The equilibrium circuit of our proposed multilayer interdigital capacitor using the model on a testing coupon is shown in Figure 3. Based on the so-called partial capacitance technique, the proposed three-layered structure for the IDC pressure can be split into three individual layers with capacitances.

The capacitance of this three layers IDC sensor can be evaluated as a function of two types of capacitance which can see in Figure 3: (1) C_I—being half the capacitance of one interior electrode relative to the ground potential and (2) C_E—the capacitance of one outer electrode relative to the ground plane next to it. Figure 3 shows the equivalent electric circuit for a structure of six electrodes having three layers above the electrode plane.

Using network analysis to evaluate the equivalent circuit of Figure 3 one finds the total capacitance between the negative and positive electrodes of a semi-infinite layer IDC-S to be equal to

$$C = (N-3)\frac{C_I}{2} + 2\frac{C_I C_E}{C_I + C_E}, \quad N > 3 \tag{1}$$

In most case, since the thickness of the electrodes is much thinner than their width, the capacitance is specified between the upper and lower half planes of the electrodes by neglecting the capacitance at the side walls. However, the thickness of the electrodes in our design is too thick to be ignored. Corrections to the equations derived by Igreja are added taking into the account of electrode thickness seen in Equations (2) and (3).

$$C_I = C_{I\_air\infty} + C_{I\_substrate} + C_{I_{steel\infty}} \tag{2}$$

$$C_E = C_{E\_air\infty} + C_{E\_substrate} + C_{E\_steel\infty} \quad (3)$$

The capacitances of the IDC unit cell with infinite layer and finite layer at interior or exterior electrodes are described using a complete elliptic integral of the first kind shown in Table I

Table I Detailed equations needed for the calculation of C_I and C_E [6]

	Interior electrodes	Exterior electrodes
Finite layer	$C_I = \varepsilon_0\varepsilon_r \frac{K(k_I)}{K(k'_I)}$	$C_E = \varepsilon_0\varepsilon_r \frac{K(k_E)}{K(k'_E)}$
	$k'_I = \sqrt{1-k_I^2}$	$k'_E = \sqrt{1-k_E^2}$
	$k_I = t_2\sqrt{\frac{t_4^2-1}{t_4^2-t_2^2}}$	$k_E = \frac{1}{t_3}\sqrt{\frac{t_4^2-t_3^2}{t_4^2-1}}$
	$t_2 = sn(K(k)\eta, k)$	$t_2 = \cosh\left(\frac{\pi(1-\eta)}{8r}\right)$
	$t_4 = \frac{1}{k}$	$t_4 = \cosh\left(\frac{\pi(1+\eta)}{8r}\right)$
	$k = \left(\frac{v_2(0,q)}{v_3(0,q)}\right)^2$	
	$q = \exp(-4\pi r)$	
Infinite layer	$C_I = \varepsilon_0\varepsilon_r \frac{K(k_{I\infty})}{K(k'_{I\infty})}$	$C_E = \varepsilon_0\varepsilon_r \frac{K(k_{E\infty})}{K(k'_{E\infty})}$
	$k_{I\infty} = \sin\left(\frac{\pi}{2}\eta\right)$	$k_{E\infty} = \frac{2\sqrt{\eta}}{1+\eta}$

Where C_I and C_E are developed using the equations and the partial capacitance technique [6]. A IDC sensor with a thick substrate of relative permittivity ε_S, top air layer of relative permittivity ε1 and the infinite material layer of relative permittivity ε_{Steel} will have their total capacitance C_I (Interior electrodes capacitance) and C_E (Exterior electrodes capacitance) given by:

$$C_I = C_{I\_air\infty} + C_{I\_substrate} + C_{I_{steel\infty}} \quad (4)$$

$$C_E = C_{E\_air\infty} + C_{E\_substrate} + C_{E_{steel\infty}} \quad (5)$$

Using the connotation shown in Figure 4 and equation (4) and (5) we have:

$$C_I = \varepsilon_0 L_C \left[\frac{K(k_{air\infty})}{K(k'_{air\infty})} + \varepsilon_{steel}\frac{K(k_{I,S\infty})}{K(k'_{I,S\infty})} + (\varepsilon_s - \varepsilon_{steel})\frac{K(k_{I,S\infty})}{K(k'_{I,S\infty})}\right] \quad (6)$$

$$C_E = \varepsilon_0 L_C \left[\frac{K(k_{air\infty})}{K(k'_{air\infty})} + \varepsilon_{steel} \frac{K(k_{E,S\infty})}{K(k'_{E,S\infty})} + (\varepsilon_s - \varepsilon_{steel}) \frac{K(k_{E,S\infty})}{K(k'_{E,S\infty})} \right] \quad (7)$$

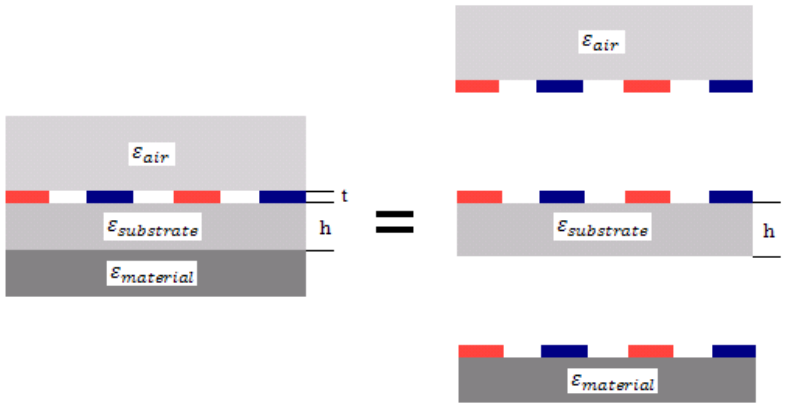

Figure.4 Splitting of the proposed three layered IDC [6]

According to our design, the capacitance value of IDC sensor changes when the crack occurs and propagates in IDC sensor, which is shown in Figure 5. This capacitance variation depends on the crack initial position, orientation and the crack length.

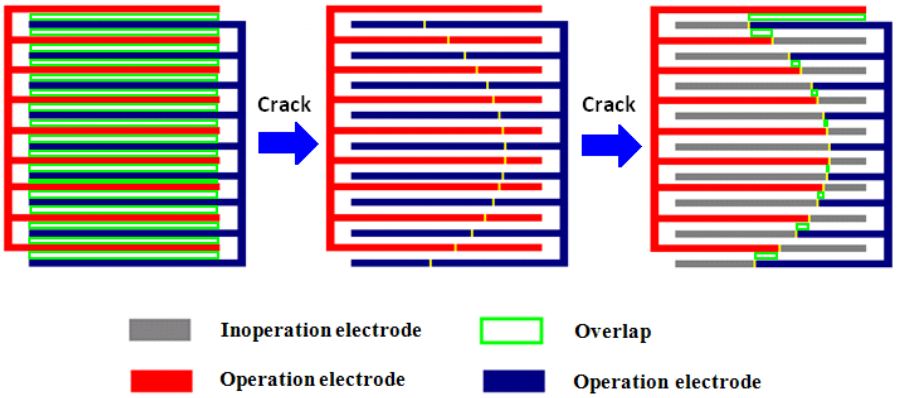

Figure.5 IDC Sensing principle

As illustrated in Figure 5, the operation capacitor of IDC sensor is varied when the crack initiates and propagates.

Table II IDC Design Parameter

Design Parameter	Symbols	Value
The number of total electrodes	NC	26
The length of each fingers	LC	23mm
Thickness of fingers	t	35um
Thickness of substrate	h	100um

The width of each fingers	w_C	500um
The gaps width between electrodes	g_C	800um

B2. Inductance estimation

Since spiral inductors provide high quality factor elements and are feasible in harsh environment applications, they are widely utilized to make resonant circuit elements for capacitive sensors in the microelectronics field.
The proposed wireless passive crack sensor has a circular inductive coil, the coil was formed by winding (8 turns) a coated copper wire (0.674mm diameter), forming a circular loop (40mm diameter).

The self-inductance of circular loop of round wire has low frequency inductance that can be estimated by [7].

$$L \approx n^2 \mu_0 R \left[\ln\left(\frac{8R}{a}\right) - 1.75 \right] \quad (8)$$

Here the loop radius is *R*, the wire radius is *a*, and *n* corresponds to the turns of the inductor. The inductance of the proposed crack sensor is 8.2*uH*. Figure 11 indicates how the coil turn and inductor radius affect inductance, for a wire radius a of 0.337*mm*

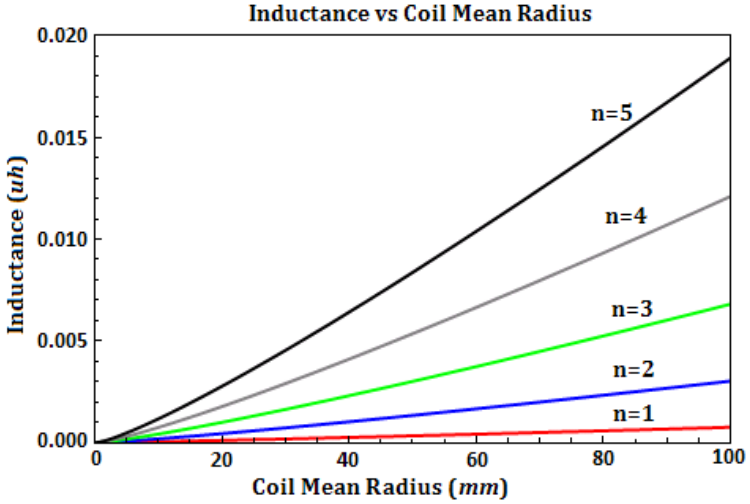

Figure.11 Inductance vs. Coil Mean Radius

D. Conclusions

This report presents a new idea and preliminary simulation of the proposed crack sensor. As the result, crack information can be retrieved and interpreted based on the received signal from the reader by the LC resonant frequency shift.

7. List of students supported and participated in this project

Graduate Students:

1. Jos é Villalobos, Department of Mechanical Engineering, UPRM

2. F. Andrés Bejarano, Department of Mechanical Engineering, UPRM
3. Ya Wang, Department of Mechanical Engineering, UPRM
4. Zhen Xu, Department of Mechanical Engineering, UPRM

Undergraduate Students:

1. Sulabel Sánchez, Department of Electrical Engineering, UPRM
2. Rogie, I. Rodríguez, Department of Mechanical Engineering, UPRM
3. Joseph Barber, Department of Mechanical Engineering, UPRM

8. List of journal and conference papers published by the results of the project

1. Rogie I. Rodriguez and Yi Jia, A wireless inductive-capacitive (L-C) sensor for rotating component temperature monitoring, International Journal on Smart Sensing and Intelligent Systems, VOL. 4, NO. 2, June 2011, pp325-337.
2. Jose G. Villalobos, Zhen Xu, and Yi Jia, IDC Based Battery-free Wireless Pressure Sensor, *Sensors & Transducers Journal, Vol. 121, Issue 10, October 2010, pp. 121-132*
3. Yi Jia, Henning Heuer, Susanne Hillmann, Norbert Meyendorf, Stray Capacitances of an Air-Cored Eddy Current Sensor", Sensors & Transducers journal, Vol.111, Issue 12, 2009, pp.25-37
4. F. Andrés Bejarano, Yi Jia, and Frederick Just, "Crack Identification of a Rotating Shaft with Integrated Wireless Sensor", International Journal on Smart Sensing and Intelligent Systems, Vol. 2. No.4, December, 2009, pp564-578.
5. Ya Wang, Yi Jia, Qiushui Cheng and Yanyuan Wang, "A Passive Wireless Temperature Sensor for Harsh Environment Applications", Sensor Journal, December 8, 2008
6. Yi Jia, Michael Heiß, Qiuyun Fu, and Nicolas A. Gay, A Prototype RFID Humidity Sensor for Built Environment Monitoring, the 2008 IITA Conference on Geoscience and Remote Sensing (IITA-GRS 2008), shanghai, December 21-22, 2008.
7. Yi Jia and Guillermo Araya, Numerical analysis of the design parameters on the performance of thin film temperature sensors, Measurement Science and Technology, Vol. (2007), pp.2268–2274
8. Dongdong Jia, Weiyi Jia, and Yi Jia, Long Persistent Alkali-earth Silicate Phosphors Doped with Eu^{2+}, Nd^{3+}, Journal of Applied Physics, Vol. 101, (2007), No.2, 023520